

國立交通大學

機械工程學系

博 士 論 文

低熱值燃料應用於環型微渦輪引擎之
實驗分析與數值模擬

Experimental Investigations and Numerical Analyses of an
Annular Typed Micro Gas Turbine using Low-heating Value Fuels

研 究 生：楊竣翔

指導教授：陳俊勳 教授

中 華 民 國 九 十 八 年 十 一 月

低熱值燃料應用於環型微渦輪引擎之
實驗分析與數值模擬

Experimental Investigations and Numerical Analyses of an Annular Typed
Micro Gas Turbine using Low-heating Value Fuel

研究生：楊竣翔

Student : Chun-Hsiang Yang

指導教授：陳俊勳教授

Advisor : Prof. Chiun-Hsun Chen

國立交通大學
機械工程學系
博士論文

A Dissertation

Submitted to Department of Mechanical Engineering

College of Engineering

National Chiao Tung University

in Partial Fulfillment of the Requirements

for the Degree of

Doctor of Philosophy

in

Mechanical Engineering

November 2009

Hsinchu, Taiwan, Republic of China

中華民國九十八年十一月

低熱值燃料應用於環型微渦輪引擎之 實驗分析與數值模擬

學生：楊竣翔

指導教授：陳俊勳教授

國立交通大學機械工程學系

摘要

為了嶄新的世代，要解決石化燃料短缺危機與符合環保規範減量二氧化碳的生成，再生能源的利用與新興能源的開發已經成為政府極力發展的能源政策，本論文透過數值模擬與實驗分析檢驗了低熱值燃料應用於擁有環型燃燒室之微渦輪引擎的可行性，研究中使用已開發完成的燃油氣渦輪引擎 MW54 作為載具，並將其以燃油為燃料的燃燒室重新改裝成為適合低熱值生質能氣體燃料之微渦輪引擎燃燒系統，

本論文包含三個部份，第一部分，本論文透過實驗分析，了解低熱值燃料應用於擁有環型燃燒室之微渦輪引擎所能產生的效能。首先為微渦輪引擎架設相關的驅動與感測裝置來完成研究用測試平台。研究中使用不同比例的 CO₂ 混合甲烷做為實驗用的低熱值燃料，透過量測得到的數據來分析與評估此引擎的效能。實驗結果顯示，微渦輪引擎最低可使用 60% 甲烷含量的燃料來運轉，而使用 90% 甲烷燃料時，發電量在 85,000 轉時達到 170W，且 70% 甲烷燃料可在 60,000 轉達到 70W。當使用 60% 甲烷燃料

時，微渦輪引擎所能產生之動力相當的低。微渦輪引擎的布雷登循環效率與發電效率可透過實驗數據的計算得知，最高分別是 23% 與 10%。

第二部分為透過套裝軟體 CFD-ACE+的應用完成了環狀微渦輪引擎在供應低熱值的燃料下，燃燒室襯孔對於燃燒室內熱流場的冷卻效應與環狀微渦輪引擎內的燃燒行為之數值模擬。分析的內容包括環狀微渦輪引擎內的流動特性、燃燒行為、熱傳導分析、化學反應與彼此之間的交互作用。模擬的結果顯示從稀釋區進入的空氣充分的發揮冷卻的效用，而此燃燒室的設計在使用低熱值燃料時，並不會在襯桶壁上產生熱點且排氣溫度都低於排氣溫度的最大容許溫度 800°C 。

第三部分為未來工作的先前研究，包括了微渦輪引擎的系統鑑別。透過實驗收集整合的數據，可以幫助我們鑑別控制系統內模擬模型的參數，系統鑑別的工作是未來設計控制系統時所必備的。本論文完成了一個使用再生性生質氣體的分散式發電系統，本系統體積小、低成本、維修容易且適合推廣於家庭用。

Experimental Investigations and Numerical Analyses of an Annular Typed Micro Gas Turbine using Low-heating Value Fuel

Student: Chun-Hsiang Yang

Advisor: Prof. Chiun-Hsun Chen

Department of Mechanical Engineering

National Chiao Tung University

ABSTRACT

The utilization of renewable energy and development of new energy sources are the present governmental energy policy to cope with the more and more stringent shortage of fossil fuels and environmental regulations for carbon dioxide reduction in the new century. This dissertation examines the practicability of low-heating value (LHV) fuel on an annular micro gas turbine (MGT) through experimental evaluations and numerical simulations. The MGT used in this study is MW-54, whose original fuel is liquid (Jet A1). Its fuel supply system was re-designed to use biogas fuel with LHV.

There are three parts in this dissertation. In the first part, experiments were completed to evaluate the combustion efficiency of an annular MGT while applying the LHV fuel. The corresponding sensors and actuators for the MGT were established to form our test stand. The methane was mixed with different ratio of CO₂ to be our LHV fuel. The measured data indicating the engine performance were analyzed and evaluated. Experimental results showed that the presented MGT system operated successfully under each tested condition when the minimum heating value of the simulated fuel was approximately 60% of

pure methane. The power output was around 170W at 85,000 RPM as 90% CH₄ with 10% CO₂ was used and 70W at 60,000 RPM as 70% CH₄ with 30% CO₂ was used. When a critical limit of 60% CH₄ was used, the power output was extremely low. Furthermore, the best theoretical Brayton cycle efficiency and electric efficiency of the MGT were calculated as 23% and 10%, respectively.

Following the experiments, the corresponding simulations, aided by the commercial code CFD-ACE+, were carried out to investigate the cooling effect in a perforated combustion chamber and combustion behavior in an annular MGT when using LHV gas. The investigation was conducted to realize the characteristics of the flow, combustion, heat transfer, chemical reaction, and their interactions in an annular MGT. The results confirmed that the cool air flows through dilution holes on combustor liners were functioning fully and there were no hot spots occurred in the liners. In addition, the exhaust temperatures of combustion chamber were lower than 1073K when MGT was operated under different conditions.

Finally, the system identification of MGT was completed for future studies. The model identification process is prerequisite for controller design research in the near future. The measured data helped us identify the parameters of dynamic model in numerical simulation. This dissertation presents a novel distributed power supply system that can utilize renewable biogas. The completed micro biogas power supply system is small, low cost, easy to maintain and suited to household use.

誌 謝

感謝恩師陳俊勳教授的悉心指導與各位審查委員的寶貴意見，感謝求學生涯中遇到的每一個人，你們帶給了我不同的成長與幫助，謝謝您。七年前，受到蔡明祺老師的提攜，讓我踏上了研究之路，碩士班的研究生涯，受馮榮豐老師的指導，讓我打好了研究所需的一切根基，也了解了學術界的生態與運作模式，之後在教授們的推薦之下，進入了交通大學博士班，加入了陳俊勳老師所領導的燃燒防火實驗室的研究團隊。

實驗室中遇到的每一個人，都帶給我不同的回憶並豐富了我的求學經歷，無敵、振稼、蕭哥謝謝你們對共同研究目標的努力；高苑莊老師、大達、文魁、文耀學長謝謝你們的鼓勵與建議；瑯原、阿貴、振忠、達叔、季哥、DC、金輝、瑋琮與實驗室的每一位，謝謝你們構築了我故事中的點點滴滴，謝謝不斷出現，但誌謝本就該充滿感謝之詞。

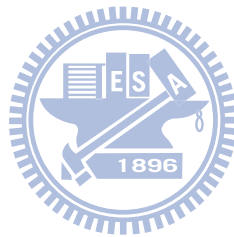
最後在此將本論文獻給支持我一切的父母、同為學位努力的二姐與我的女友，謝謝你們。

CONTENTS

摘要	i
ABSTRACT	iii
誌謝	v
CONTENTS	vi
List of Tables	ix
List of Figures	xi
Nomenclature	xii
Chapter 1 Introduction	1
1.1 Motivation	1
1.2 Literature Review	3
1.2.1 Numerical simulation	3
1.2.2 Micro gas turbine	7
1.2.2 Micro gas turbine modeling	12
1.3 Scopes of the present study	14
Chapter 2 Experimental investigation	17
2.1 Briefing of the proposed micro gas turbine system	17
2.1.1 Transmission System	18
2.1.2 Fuel supply	19
2.1.1 Start system	19
2.1.1 Lubrication	19
2.2 Experiment layout	20
2.3 Measurement instrumentation	20
2.3.1 Data Acquisition	20
2.3.2 Temperature measurement	22
2.3.3 Turbine RPM measurement	22
2.3.4 Fuel pressure measurement	22
2.3.5 Fuel flow rate measurement	23

2.4 Test stand operating procedures	23
2.5 Parameters of tests	25
2.6 Uncertainty Analysis	25
2.6.1 The Asymmetric Uncertainties of Thermocouple	26
2.6.2 Uncertainty Analysis of mass flow controller	27
2.6.3 The Experimental Repeatability	27
Chapter 3 Numerical analyses	30
3.1 Domain descriptions	30
3.2 Governing equations.....	30
3.3 CFD-ACE+ software	36
3.4 Numerical method	36
3.5 Boundary conditions.....	36
3.5.1 The inlet boundary conditions	37
3.5.1.1 Air inlet boundary conditions of combustor	37
3.5.1.2 Fuel inlet boundary conditions of combustor	39
3.5.2 The outlet boundary conditions.....	40
3.5.3 The symmetry boundary conditions	40
3.5.4 The interface boundary conditions	40
3.5.5 Wall boundary conditions.....	40
3.6 Computational procedure of simulation	40
3.7 Grid-independence test.....	41
Chapter 4 Dynamic Model of MGT for Control Strategy	47
Chapter 5 Results and Discussions	49
5.1 Experimental results and discussions	49
5.1.1 Tests using various fuels with no load.....	49
5.1.1.1 Pressures and volume flow rates of fuel in the MGT ...	50
5.1.1.2 Temperature of unloaded MGT.....	52
5.1.1.3 Thermal efficiency	53
5.1.2 Testing MGT with generator	54
5.2 Numerical Simulation results and discussions	56
5.3 Extended studies results	61

5.3.1 System identification.....	61
Chapter 6 Conclusions and Future Works	66
5.1 Conclusions	66
5.2 Future Works	67
References	68



List of Tables

Table 2.1 Specifications of the data acquisition modules	21
Table 2.2 Experimental repeatability for volume flow rate for various fuels...	29
Table 3.1 Sutherland's law coefficients of dynamic viscosity	43
Table 3.2 JANNAF coefficients of gas specific heat	44
Table 3.3 Properties of solid liner	45
Table 3.4 Boundary conditions of combustion chamber.....	45
Table 3.5 Grid test results of different grid densities for numerical simulation	46
Table 4.1 Simulation results for four-step reaction mechanism.....	63



List of Figures

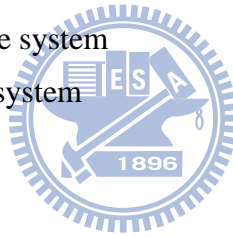
Fig. 1.1 The structure of project.....	73
Fig. 1.2 The basic structure of the MGT generator.....	73
Fig. 1.3 Pictures of the adopted micro gas turbine.....	74
Fig. 2.1 Pictures of the major parts in MGT (a) Compressor; (b) Combustion chamber; (c) Turbine wheel	75
Fig. 2.2 Pictures of experimental facilities in proposed MGT system.....	75
Fig. 2.3 Schematic of experiment layout	76
Fig. 2.4 Pictures of data acquisition devices	77
Fig. 2.5 Pictures of sensors and actuators for the proposed MGT system.....	78
Fig. 2.6 The relationship of temperature and error	79
Fig. 2.7 Experimental error bars for CH ₄ :CO ₂ mixing ratios	80
Fig. 3.1 The simplifying procedure of model domain illustrated by software Solid Works.	81
Fig. 3.2 The configurations of a sub-chamber	82
Fig. 3.3 The size specification of sub-chamber.....	82
Fig. 3.4 Grids generation for numerical computation.....	83
Fig. 4.1 Simulation model of micro gas turbine in SIMULINK.....	84
Fig. 5.1 Volume flow rate for fuels with LHV fuels at various RPMs	85
Fig. 5.2 Compressor speed vs. volume flow rate of CH ₄ with different concentrations of methane fuels.....	86
Fig. 5.3 Temperatures at different positions in the MGT (a) Fuel with 90% CH ₄ ; (b) Fuel with 80% CH ₄ ; (c) Fuel with 70% CH ₄ ; (d) Fuel with 60% CH ₄	88
Fig. 5.4 (a) Combustion chamber (oil); (b) Combustion chamber using 70% CH ₄ (gas).	89
Fig. 5.5 Brayton cycle efficiency of different compressors speed with different concentrations of CH ₄	90
Fig. 5.6 Output power for different generator rotation speeds with different LHV fuel.....	91
Fig. 5.7 Simulation results of applying 60% methane fuel at rotation speed 45000RPM.....	92
Fig. 5.8 Distribution of temperature for different concentration of methane at	

45000 RPM.....	93
Fig. 5.9 Distributions of CH ₄ mass fraction for different concentration of methane at 45000 RPM.....	94
Fig. 5.10 Distributions of O ₂ mass fraction for different concentration of methane at 45000 RPM.....	95
Fig. 5.11 Velocity vector of flow field for different concentration of methane at 45000 RPM.....	96
Fig. 5.12 Curved chart with different methane concentration and different compressor speed	97
Fig. 5.13 Maximum temperature at combustor outlet for different fuel.....	98
Fig. 5.14 Numerical result of output power for different generator rotation speeds with 90% CH ₄	99
Fig. 5.15 Numerical result of turbine outlet temperature versus experimental time.....	100



NOMENCLATURE

A	Pre-exponential factor
C_p	Specific heat
D_h	Hydraulic diameter
h_i	Enthalpy to different species
h_0	Total enthalpy
I	Turbulence intensity
k_r	Reaction rate constant
k	k-equation for turbulent model
\dot{m}	Volume flow rate
m_i	Mass flow rate to different species
n	Temperature exponent
P	Pressure
P_{out}	Pressure of mass flow controller outlet
Q_L	Heat transferred out of the system
Q_H	Heat transferred into the system
S_h	Energy source
T	Temperature
T1	Temperature of compressor inlet
T2	Temperature of compressor outlet
T3	Temperature of turbine inlet
T4	Temperature of turbine outlet
u, v, w	Velocity components in the (x, y, z) system of coordinates
W	Actual work of system
ρ	Density
τ_{ij}	Stress tensor component
ε	Dissipation rate
η_{th}	The efficiency of standard Brayton cycle
$\eta_{electric}$	Electric efficiency



Chapter 1

Introduction

1.1 Motivation

The greenhouse effect is an international problem. Controlling emissions of greenhouse gases is an important environmental goal. In response, the Taiwanese government has prioritized utilization of renewable energies and the development of new energy sources. As a large amount of biogas can be derived from bio-waste, this fuel source is currently favored in Taiwan. Marsh gas is comprised of approximately 50% methane. Although methane is lighter than both air and natural gas, it has similar thermal and physical properties. Methane generated from garbage, which is an air pollutant, can be used as fuel. Notably, generating electrical power using methane gas can reduce the emission of a greenhouse gas and simultaneously produce electrical power.

Recently, people pay intensive attention to find new sources of energy, to save energy, and to raise the consciousness of protecting environment. National Science Council has awarded our laboratory a three-year research project from 2006 to 2008. Fig. 1-1 shows the infrastructure of the project, which is divided into four subprojects. The goal of the *subproject 1* is to increase the utilization efficiency of biogas by removing H₂S and improving the power generation rate. The CO₂ emitted from biogas will also be reduced by chemical methods. The focus of the *subproject 2* is to produce the biodiesel from high lipid-content algae in wasted CO₂. The purpose of the *subproject 3* is to develop a process that may effectively produce hydrogen from primary products of biomass, including alcohols, methane of subproject 1, and biodiesel of subproject 2. The

subproject 4 develops a micro gas turbine (MGT) which could be used to drive a generator to produce the electricity by modifying the burner from a liquid-fuel burning gas turbine system into a gas-burning one to generate the combustion power. It is a co-generation process, which can be one of the potential candidates for the distributed power supply systems.

The research of this study focuses on subproject 4. The market assessments in 2000 identify several potential types of power applications for MGT, including continuous generation, premium power, mechanical drive, and combined heat and power. Gas turbine is a system device supplying jet propulsion and/or power. Gas turbine can make the much stronger gas flows than a piston engine during the common continuous processes of running. The strength of gas flow can be changed to axial power by a gear box with a turbine. If the axis is connected to a generator, the gas turbine can be used to generate electric power.

MGTs offer a lot of potential advantages over other technologies for small-scale power generation. There are less moving parts in a MGT, so there would be less friction loss, lower vibrating, lower electricity costs, high reliability and less maintaining cost. Besides, the size of a MGT is smaller and its weight is lighter so it can generate a high power-to-weight ratio and lower emissions.

It can be located on sites with limited space to produce power, and the waste heat recovery can be used to improve more than 80% efficiencies. Compared with the reciprocating engine, MGT is also more efficient because of its simple structure and less moving parts. In terms of power density, gas turbine is also better than the reciprocating engine. Combining the MGT with the methane gas could generate electric power, and the methane gas could replace the traditional

oil fuel.

The methane gas is obtained from the purified marsh gas through bio-process. Owing to the limitation of present biochemical technique, there still exists a little amount of impurity gases, such as carbon dioxide (CO₂), which cannot be removed completely. It would dilute the concentration of pure methane gas so that the MGT is not easily to operate.

In addition to the concern of heat value, the phase state of liquid is different from that of gas. This difference would cause the mismatch of the gas turbine system. The components of gas turbine can be roughly divided into three parts: compressor, turbine wheel and combustion chamber. With introducing the low heating value (LHV) fuel, its total mass flow has a much greater mass fraction of air than that with a liquid fuel. Consequently, the reaction behaviors in combustion chamber are also changed. Therefore, the gas turbine should be adjusted to be able to apply LHV fuel. When the system is microminiaturized, it can be used in many kinds of electric power demands, such as electric vehicles, motorcycles, portable generators, and even PCs and laptops.

1.2 Literature Review

1.2.1 Numerical simulation

Much previous research on micro gas-turbine had made effort to improve the combustor efficiency or to bring up novel designs. Most design factors and coefficients were obtained from experiments and designers' experience. Especially, the combustion chamber is the most heavily thermal load part in a turbine engine and its service life is normally very short. Since very limited data can be obtained from expensive engine tests due to its serious work environment,

a well founded numerical simulation will lower the process cost between design and experiment layout.

As powerful computing technologies are continuously and rapidly improved, computational fluid dynamics (CFD) methods have become a feasible tool in the aero-turbine industry. Many of the previous CFD models of gas turbine combustors included only calculation of reacting flows within the combustor liner while assuming profiles at the various liner inlets [1-5].

Lawson [1] calculated the reacting flow inside the combustor liner. A structured single-block grid was used in this study. Lawson was able to successfully match the calculated radial temperature profile at the combustor exit with experimental data, and then used the calibrated CFD model to predict the radial temperature profile that resulted from different cooling and dilution air patterns. Lawson used a one-dimensional code to predict flow splits, and a two-dimensional CFD model to predict the flow profile at the exit plane of the swirl cup. This profile was then applied as a boundary condition in the 3D model.

Fuller and Smith [2] predicted the exit temperature profiles of an annular direct flow combustor that were in fairly good agreement with measurements. They used a structured multi-block grid in their calculations, which was essential for modeling complex geometries. They also used a two-dimensional model to provide the boundary conditions at the exit plane of the swirl nozzle.

Gulati et al. [3] devoted to study a 3 dimensional full-scale 10-cup combustion sector with double-annular. Calculations were carried out for the same geometry and operating conditions using the CONCERT-3D CFD code. A single block structured grid was used to calculate the flow inside the combustor liner. The predicted exit plane mean and RMS temperature, and mole fraction of the major species were then compared with the measured data, and were found to

be in fair agreement. The effects of various inner/outer dilution air jets combinations on the exit plane mean temperature (radial distribution of the circumferentially averaged temperature) and major species mole fractions were also studied and compared with the experimental results. The calculated results were found to recover the trends of these geometry variations fairly well.

Danis et al [4] used the proprietary code CONCERT to calculate the inner chamber flow of five modern turbo-propulsion engine combustors. The N-S equations were solved for turbulent reacting flows, including spray modeling. The 3D CFD models were first calibrated based on design database for one combustor. The anchored models were then run successfully for the other four combustors. A structured single-block grid was used in this research with suitable meshing around the internal obstacles. Two-dimensional results for the exit velocity profiles, along with measured spray quality, were used as a swirl cup inlet condition for the 3D calculations. Consequently, the turbulence properties at the swirl cup in the 3D calculations were calibrated using design database.

Lai [5] modeled the inner chamber of a gas turbine combustor similar to that of the Allison 570KF turbine used by the Canadian Navy. A 22.5 deg periodic sector of the combustor was modeled using a structured multi-block grid. Lai included the swirled passages in his model, which was an important step in reducing the uncertainty in the boundary conditions. The simulation results for the combustor flow fields in this research didn't compare with the experimental data.

In a recent study, Gosselin et al. [6] simulated steady, 3D turbulent reacting flows with liquid spray, in a generic type gas turbine combustor using a hybrid structured/unstructured multi-block grid. The commercial FLUENT code was used in this study. The calculation allowed for detailed combustor geometry, including the inner chamber, external channel, and the various liner film cooling

holes and dilution ports. The N-S equations were solved using the $k\text{-}\epsilon$ /RNG turbulence model and the PDF turbulent kinetic energy reaction rate model. The calculated results for the gas temperatures, mass functions of CO/CO₂, and velocity fields were compared with experimental measurements. However, no prediction of the wall temperature was included in this work.

Ho et al. [7] proposed a prototype simulation modeling of annular combustor chamber with two-phase flow field. Ho's research utilized the commercial code, INTERN, which was developed and technically supported by NERC.

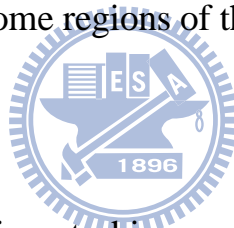
Crocker et al. [8] used a software CFD-ACE to simulate a combustor model from compressor diffuser exit to turbine inlet. Their model included an air-blast fuel nozzle, dome, and liner walls with dilution holes and cooling louvers. The comprehensive model made it possible to predict flow splits for the various openings into the combustor liner and to remove the guesswork required for prescribing accurate boundary conditions for those openings. The simulation was combining the conjugate heat transfer analysis and the gas radiation. The coupled modeling which could provided a direct prediction of liner wall temperatures including both inside and outside the liners. Non-luminous gas radiation added approximately 40K to the hot side of metal wall temperature.

Priddin and Eccles [9] also demonstrated the capability of full-combustor structured-mesh analysis, and highlighted the usefulness of a streamlined CAD-to-grid process utilizing parametric solid models. Birkby et al. [10] developed a description of an analysis of an entire industrial gas turbine combustor, in which the premixing fuel nozzle was coupled with the combustion chamber. Snyder and Stewart [11] developed a CFD analysis on an entire PW6000 combustor domain to predict temperature distribution at the combustor exit and compared the CFD result with the full annular rig-test data.

However, all aforementioned studies on “full combustor” omitted cooling devices or simplified cooling holes to slots.

Li et al. [12] proposed a fluid-solid coupling simulation in an aero-engine annular combustor to investigate the integrated contribution of combustion and cooling to the thermal load in a completely structure annular tube. The reliability of the simulation was demonstrated by comparing calculated combustor exit temperature distributions with profiles of the rig-test measurements. The predicted profile was in a quite good agreement with the rig-test data indicating that the proposed CFD analysis could explore the major performance of the fluid flow and combustion in the gas turbine combustor. The simulation results showed that the combination of local combustion and shortage of coolant might lead to film cooling/protection failure in some regions of the combustor.

1.2.2 Micro gas turbine



Wen [13] studied the micro turbine generator system that introduced the experimental foundation for a 375hp micro turbine generator system, which included inlet and exhaust section, testing frame, operating control system and measurement system. Besides, the operating control systems of the micro turbine generator system that included starter system, fuel supply system, lubrication system, ignition system and secondary air supply system of combustor had to be set up. Additionally, the measurement devices and data acquisition system needed to measure the engine baseline performance were completely designed and constructed.

Wang [14] tested and analyzed a 150 kW micro turbine generator set with twin rotating disk regenerators. Using the PC-based data acquisition system, the engine speed, turbine inlet temperature, exhaust temperature, compressor inlet

and discharge pressure, and fuel flow rate were all measured. The generator set was tested by using load bank to establish the baseline performance including temperature, pressure, horsepower, fuel consumption, and speed. He used the software program GasTurb to predict the performance of the micro turbine generator set in different operating conditions in order to compare with the test results. The thermal efficiency of 28% was predicted at full load with regeneration while the no regeneration case only had 14% thermal efficiency.

There are a few companies currently working on micro-turbines in the 25-250 KW range. To understand the state of industry, a brief overview of some of the companies and their products are discussed. The name “Capstone” [15] often arises in conversations about micro-turbine generators. One of their smaller generators is a 30 KW load-following device that is set up for combined heat and power (CHP). The device is 26% electrically efficient and boasts one moving part, namely the compressor-turbine-generator shaft. From the heating and cooling end, the unit emits 85 KW of thermal energy that can be used to power an absorption chiller or heat exchanger. One major advantage of this device is that it is a relatively quiet machine, which operates at 65 db when it is measured 10 m away. Capstone has also developed a large 65 KW device that is 29% electrically efficient and outputs 78 KW of thermal energy for CHP applications. It has a total fuel efficiency of 64%.

Bowman Power [16] has an 80 KW device that outputs between 136 and 216 KW of thermal energy. It is rated at 70 db at 1 meter away. This unit includes a boiler for utilizing the waste heat to produce steam for CHP applications. It also has the flexibility to operate with a multitude of fuels such as natural gas, propane, and butane. The rather important parts of this generator are the power electronics and computer controls that regulate the engine and condition the

signal from the generator to maintain waveform quality. To complete the overviews of the companies, Ingersoll-Rand has also developed a 70 KW device that is 29% electrically efficient and it is rated at 78 db at 1 m away and 58 db at 10 m away.

Recent advancement in micro-fabrication technology has opened up a new possibility for micro-power generation machines. Those are often referred to as Power MEMS. A famous example of Power MEMS project is the Micro-engine Project at Massachusetts Institute of Technology (M.I.T.).

M. I. T. [17] was devoted to a micro-engine project, which tended to establish the technical foundation of the MEMS-based gas turbine for man-portable power generators and micro-jet engines for micro-aerial vehicles (MAV). At M.I.T., researchers were challenged to develop a gas turbine generator only by using micro electromechanical systems (MEMS) fabrication technologies. This was a technology based on deep reactive ion etching (RIE) of silicon; hence the geometry of the product was limited to near-2-dimensional shape.

Wu et al. [18] proposed a computational model to stabilize the combustion in a MGT engine. Comparing to the original design of M. I. T., an extra wafer layer of micro channel was added to regulate the fluid flow velocity distribution and direction near the combustor entrance. As a result, the fuel/air mixture flow velocity decreased along the flow path before entering into the combustion chamber. This special flow velocity distribution concluded that under the conditions of higher equivalence ratio, lower heat loss, or higher mass flow rate, the flame could be stabilized in the combustor with the improved design, whereas the flame would flash back and burn in the recirculation jacket or be blown out from the combustor with the original design. The simulation results

also demonstrated that the new design may provide a micro-combustor with higher power density by significantly extending stable operating ranges, such as the fuel/air mixture mass flow rate range.

Shan et al. [19] emphasized the design, fabrication and characterization of a silicon-based micro combustor for gas turbine engines. The micro combustor consisted of seven-layer microstructures made from silicon wafers, and it adopted a novel fuel–air recirculation channel to extend gas flow path. Numerical simulations, which was based on computational fluid dynamics (CFD) demonstrated a guideline for selecting parameters during combustor operation and indicated that the flame temperature inside the combustor reached 1700 K. Experimental investigations demonstrated that a stable combustion could be sustained inside the micro combustor. The highest temperature measured at the edge of the combustor exit had reached 1700 K, and the average temperature recorded near the exit ranged from 1200 K to 1600 K.

However, the limitation in the geometry will penalize the performance of the MEMS-based gas turbines. Macro-scale gas turbines usually have strongly three dimensional shapes to achieve optimal aerodynamic performance.

Jan et al. [20] studied a single-stage axial micro-turbine with a rotor diameter of 10mm. This turbine was a first step in the development of a micro-generator that produced electrical power from fuel. The micro turbine developed at M. I. T. which manufactured using lithographical process was a radial turbine with a rotor diameter of 4mm. Consequently, the micro turbine developed by Jan used an axial-radial turbine with a diameter of 12 mm. A 10 mm diameter axial micro turbine with generator was developed and successfully tested to speed up to 160,000 rpm. It generated a maximum mechanical power of 28W with an efficiency of 18%. Power and efficiency were mainly limited by

the tolerable maximal speed of the ball bearings. When coupled to a small generator, the proposed system could generate 16W of electrical power, and the efficiency for the total system was 10.5%.

Isomura et al. [21] studied the micromachining gas turbine, which was developed by Tohoku University. In the MGT, the heat transferring from the high temperature components to the low temperature, such as the combustor and the turbine for the former and the compressor for the latter was much higher because the distance separating the high and low temperature components was closer than that of the general turbine. So, the temperature gradient became large if the highest and lowest temperatures in the turbine were the same. Therefore, the MGT could not be directly diminishing the scale as the same structure of the macro-scale gas turbine.

The aforementioned gas turbines have a separate geometry between combustion chamber and compressor-turbine axle. The relatively huge size and the difficulty of constructing equipment force us to consider an annular type combustion chamber in order to construct a portable distribute power system.

Shiung [22] found that it is always difficult to accurately arrange the inlet air distribution in designing a micro engine combustor, because the suitability of the conventionally recommended C_d (discharge coefficient) based on large and small engine is questionable for micro-engine. The relationship between C_d and dynamic pressure ratio K , for micro-engines was examined through experiment under the condition that K was from 1 to 4. Then, with the aid of the oil flow techniques and pressure data, the inlet air distribution could also be estimated.

Li [23] manufactured the model chamber, which was geometrically identical to prototype chamber, in the cold-flow tests. It was found that the pressure loss of flow through the liner hole was about 3% of the total pressure. These

information were helpful to modify the chamber design. In the firing tests, it discussed the mixing effects by changing the fuel injection direction and by controlling the numbers of swirl holes. The results showed that upstream fuel injection mode did play well in the short chamber length compared to the side fuel injection mode.

Bio-mass as a renewable resource and an environmental friendly energy carrier is assigned an increasing importance for future energy supply. So far bio-mass have mainly been the focus of an alternative fuel for gas turbine engines.

Peirs *et al.* [24] utilized a micro turbine with a rotor diameter of 10mm to generate electrical power using liquid fuel. The tolerable maximal speed of ball bearings was the primary constraint on both power generated and efficiency. When attached to a small generator, the turbine generated 16W of electrical power; overall system efficiency was 10.5%. The rotor was tested at speeds up to 130,000 RPM with compressor air at 330°C. The micro turbine was small enough that it could be widely applied; however, some researchers have questioned whether it can use gaseous rather than liquid fuel.

Yamashita *et al.* [25] examined MGT under experimental conditions using fuels with low-heating value. Their simulations used liquefied petroleum gas (LPG) diluted with N₂. The efficiencies of all system components were based on temperature and pressure measurements. The proposed MGT system was successfully operated using a fuel with a heating value that was 43% of that of LPG, indicating that, when using fuels with LHVs, the combustor requires no modifications. However, the MGT system in this study was large.

1.2.3 Micro gas turbine modeling

The studies in the control of gas turbine have been a subject since the gas-turbine engines have been widely adopted as peak load candidates for electrical power generation. In controlling the gas-turbines in their steady state, it is very important to stabilize the turbine rotor speed and exhaust temperature to rated values under a perturbed load torque.

A thorough introduction to gas turbine theory was provided in the book of Cohen et al. [26]. There also existed large literatures on the modeling of gas turbines. Model complexity varied according to the intended application. Detailed first derivation modeling based upon fundamental mass, momentum and energy balances was reported by Fawke et al. [27] and Shobeiri [28]. These models described the spatially distributed nature of the gas flow dynamics by dividing the gas turbine into a number of sections. Throughout each section, the thermodynamic state was assumed to be constant with respect to location, but varying with respect to time. Mathematically, the entire partial differential equations (PDE) model description was reduced to a set of ordinary differential equations that facilitated easier application within a computer simulation program. Much simpler models result could be achieved if the gas turbine was decomposed into just three sections corresponding to the main turbine components, i.e. compressor, combustor and turbine [29]. Al-Hamdan [30] also presented a modeling approach procedure to the gas turbine engine based on aero thermodynamic laws. Overall performance of the complete gas turbine engine was mainly determined by the main components including the compressor, the combustion chamber and the turbine. Instead of applying the fundamental conservation equations, as described above, another modeling approach was to characterize gas turbine performance by utilizing real steady state engine performance data [31]. It was assumed that transient

thermodynamic and flow processes were characterized by a continuous progression along the steady state performance curves, this was known as the quasi-static assumption. The dynamics of the gas turbine, e.g. combustion delay; motor inertia, fuel pump lag, etc. were then represented as lumped quantities separating from the steady-state performance curves. Rowen proposed a simple models result which was further assumed that the gas turbine was operated at all times close to rated speed [32]. The model included a simple cycle and single-shaft gas turbines with inlet guide vane opened. Hannett et al. [33] reported that the model structure provided by Rowen was found to be adequate by simulation results. From the viewpoint of control scheme, Rowen and Hannett both used conventional fixed-gain proportional integral controllers for speed, temperature and acceleration controllers.

In [34] and [35], nonlinear lumped parameter mathematical models of gas-turbine plants were described and decoupling control systems, which operated with no interactions between speed and exhaust temperature loops were proposed. In order to design the decoupling controller, precise dynamic gas-plant mathematical models and accurate transfer functions of turbo-gas were required, which were difficult to attain without various experiments and deep expertise.

1.3 Scopes of the present study

This dissertation investigated the effects of using fuels with LHV on the performance of an annular MGT experimentally and numerically. The MGT adopted in this study was modified from a MW54 MK III, which is shown in Fig. 1.3(a). The original liquid fuel supply piping of this turbine engine was

bifurcated into both the lubrication system for bearing and the liquid fuel system for combustion chamber. Figure 1.3(b) shows the feature of the engine that the bifurcation point is outside the engine case. This feature was the reason why we chose this engine, because such position of bifurcation point made the modification of fuel system easier.

This dissertation consisted of three parts. The first part of this study was experimental works that evaluated the combustion efficiency of an annular MGT while applying the LHV fuel. In the beginning of the experiment, the Jet A1 oil-fuel used gas turbine engine, WREN MW54, was modified to construct our gas-fuel used MGT system. LHV fuel used in this experiment was CH_4 mixed with CO_2 . The CO_2 was mixed in the LHV gas because in reality the bio-gas usually contains some impurity gases, due to the limitation of present biochemical technique that can't obtain very pure methane gas from the purified marsh gas. The experiment results were used to observe and calculate the efficiency of the MGT under the different combinations of parameters, including the mixing ratio of the CO_2 , rotation speed of compressor wheel, pressure of fuel, and mass flow rate of the fuel. It is well known that the impurities of gas will dilute the concentration of pure methane. This dissertation tries to find the optimal operating condition to our proposed MGT to reach maximum combustion efficiency. Additionally, a remote control panel based on LabVIEW was established to construct a user-friendly monitor interface.

Since the detailed flow field and temperature distribution inside the combustion chamber are hard to measure through experiment while the MGT is running. In the second part, the corresponding simulations, aided by the commercial code CFD-ACE+, were carried out to investigate the cooling effect in a perforated combustion chamber and combustion behavior in an annular

MGT when using LHV gas. The main purposes are to confirm that there were no hot spots occurred in the liners and the exhaust temperatures of combustor were lower than 800°C when MGT is operated under different conditions. The author found that there has been scarce published research on using the LHV fuel in an annular MGT numerically, except Yang et al. [36] had completed a numerical simulation process and model for a combustion chamber of the MGT with CFD-ACE+. Numerically, this dissertation first lightly modified the pre-existing numerical model for a much exact geometry to fit the existing facilities. A reliable steady state simulation result could help researchers to avoid inappropriate chamber design, which could cause hot spots on the chamber liner or could make the temperature of exhaust gas exceed the maximum allowable temperature that the turbine wheels can tolerate.

In the third part, the system identification of MGT was completed for future studies. The model identification process might be needed before the controller design research in the near future. The model identification process is prerequisite for controller design research in the near future. The measured data helped us identify the parameters of dynamic model in numerical simulation. This dissertation presents a novel distributed power supply system that can utilize renewable biogas. The completed micro biogas power supply system is small, low cost, easy to maintain and suited to household use. Finally, possible extensions of this study were suggested in the Future works section.

Chapter 2

Experimental investigation

2.1 Briefing of the proposed micro gas turbine system

The MGT shown in Fig. 2.1 is basically composed of compressor (Radius: 27mm) [Fig. 2.1 (a)]; combustion chamber (Length: 52.4mm, Radius: 38mm) [Fig. 2.1 (b)]; and turbine wheel (Radius: 25mm) [Fig. 2.1 (c)]. The compressor compresses the incoming air into high pressure. The combustion chamber burns the fuel as well as produces high-pressure and high-velocity production gases. The turbine is energized by the high-pressure and high-velocity gas flowing from the combustion chamber. The most common shaft design in a MGT is the single shaft design that a radial centrifugal compressor and turbine are attached to a shaft which was also adopted in this study. Generally, the micro turbines demonstrate the following characteristics:

- Single stage radial compressor and turbine
- Low pressure ratio which is typically from 2 to 4
- High rotor speed which is often up to hundred thousands RPM
- Minimal demand for cooling systems of rotor and turbine vanes
- Heat recovering of exhaust gas for air pre-heating
- Low cost of production

The MGT engines are optimized to generate large quantities of hot gas and the gas would be directed to pass through a second stationary guide vane and 2nd turbine, which is mounted on a separate shaft. The 2nd turbine only drives the load and it is considerably larger in diameter than the 1st stage. The 2nd turbine

turns slower and, with large blades, can absorb a large amount of energy from the gas passing through it. This enables high torque to be produced at an RPM which is relatively easy to provide further reduction to suit the application. This configuration of two shafts allows considerable mismatch to be tolerated between power turbine and load. The heart of the power unit is a single stage gas turbine using centrifugal compressor and axial turbine. Power is drawn from the exhaust by a second turbine which supplies the drive to the propeller via the gearbox.

2.1.1 Transmission System

The MGT thermal system is very similar to heavy duty turbines. However, due to the lower inertia of the compressor-turbine-generator shaft, it easily gets a high rotation speeds and may reach 100,000 rpm. Consequently, the MGT usually uses gear speed reducers to diminish the rotation speed to match the AC power grid frequency of the power generator. The gearbox adopted in this study consists of a large power turbine which drives the exhaust gas from the gas generator engine and reduction gear [Fig. 2.2(a)]. The power turbine is mounted on a shaft running in high temperature bearings. Lubrication and cooling for these bearings comes from a fuel takeoff system supplied via a tube mounted above the engine, feeding via the rear of the gearbox. The input shaft drives a gearbox comprising a two stage reduction using helical gears, fully hardened for long life. The gear box lubrication system is “wet sump” that holds the oil within the gearbox and the oil circulates by the action of the gears and requires no external oil tank or services. The gearbox is charged with 20ml of automobile transmission oil. In normal use the oil needs replacement every 20 hrs continuous running or 120 times start-up.

2.1.2 Fuel supply

A 20 Kg steel cylinder which had mounted a valve to control the value of the pressure gauge was adopted in this study [Fig 2.2(b)]. A 1/8 inch Teflon pipe was used to connect the cylinder to the MGT because the pipe is heat-resistant. The advantage of using the cylinder is that the cylinder is easy to replace while the gas is run out and easy to change with different fuels for the experiment.

2.1.3 Start system

A blower was adopted to replace the start motor. The functions of the blower were pushing the compressor of MGT rotate and supplying enough air to mix with gaseous fuel in the MGT [Fig 2.2(c)]. Additionally, the spark plug was modified to ignite the fuel more easily. The modified spark plug could be activated with a 1.5V~3V battery or a voltage regulator. If the voltage is too high, the spark plug would fail.

2.1.4 Lubrication

The MGT works at a very high rotational speed, so the lubrication system is very important. In the original system the lubricating oil is pre-mixed with the oil fuel. When the fuel emits to combustion chamber, the lubricating oil and gas would splash to the bearings. Fig 2.2(d) shows the lubrication oil in the study.

In this study, when the MGT was modified to use gaseous fuel, the lubricating oil could not be pre-mixed with the gaseous fuel. Thus, the lubricating oil pipe should be an independent component. The lubricating oil would be emitted to the bearings directly by a pump that was controlled by a digital program. The program was scheduled to pump the lubricating oil every

few seconds in order to protect the bearings.

2.2 Experiment layout

The experiment layout is shown in Fig. 2.3(a). Figure 2.3(b) shows the transmission gear box and generator, which are placed on a test frame made of 6061 aluminum alloy. Each part is fixed onto the frame. The generator is a commercial product, which was taken from a motorcycle [37]. The generated current was rectified to direct one for commercial use and the load was a set of high-power headlight, which is about 200W. The blower used to drive the MGT was connected to the MGT air inlet via a rubber tube. When the MGT reaches stable RPM, the rubber tube was removed and the turbine wheel kept rotating by absorbing power from the air combustor. The generator was connected to the MGT via a transmission gearbox, which transforms the power; generated by the MGT; into axial work. This axial work drove the generator to produce electrical power. Fuel pressure and flow rate at inlet nozzles of the combustion chamber can be adjusted using a pressure valve and flow meter. The rotational speed of the MGT was measured using an induction tachometer installed close to the compression fans. The temperatures at the compressor inlet and outlet, turbine inlet and outlet and exhaust were measured using thermocouples installed on the MGT. All measurement data were stored on disk via a laptop-controlled data-acquisition system.

2.3 Measurement instrumentation

2.3.1 Data Acquisition

Data acquisition is the process of gathering or generating information in an automated fashion from analog and digital measurement sources such as sensors and devices under test. Data acquisition uses a combination of PC-based measurement hardware and software to provide a flexible and user-defined measurement system. Oftentimes, the researcher must calibrate sensors and signals before a data acquisition device acquires them. National Instruments [38], a leader in PC-based data acquisition, offers a complete family of proven data acquisition hardware devices, and powerful and easy-to-use software that extends to many languages and operating systems. NI CompactDAQ delivers fast and accurate measurements in a small, simple, and affordable system. A CompactDAQ Chassis shown in Figure 2.4(a), which is a product of NI company was adopted because of the following advantages: Plug-and-play installation and configuration, AC power supply and USB cable connect, mounting kits available for panel, enclosure, DIN-rail and desktop development, A380 metal construction, more than 5 MS/s streaming analog input per chassis, and Hi-speed USB-compliant connectivity to PC. Different types of signal process modules were chosen to complete the data acquisition system, including NI 9203 Analog Input Module, NI 9211 Thermocouple Differential Analog Input Module, NI 9263 Analog Output Module, and NI 9215 Simultaneous Analog Input. All of the modules are shown in Fig 2.4(b-e) and the specifications of these modules are shown in Table 2.1.

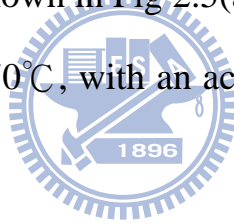
Table 2.1 Specifications of the data acquisition modules

Model	Signal Type	Channels	Max Sampling Rate	Resolution	Signal Input Ranges

NI 9203	Current	8	500 k	16 bits	±20 mA
NI 9211	Thermocouple	4	15	24 bits	±80 mA
NI 9263	Voltage	4	100 k	16 bits	±10 V
NI 9215	Voltage	4	100 k	16 bits	±10 V

2.3.2 Temperature measurement

The thermocouple probes were set up at the compressor outlet, combustion chamber, turbine wheel outlet, and nozzle outlet in order to observe the combustion situation. The exhaust temperature of the MGT engine was approximately 600-800°C which could be obtained from the numerical results. Therefore, a K-typed Chromel (chromium-nickel alloy) alumel (aluminium-nickel alloy) thermocouple shown in Fig 2.5(a) was used to measure temperature in the range of -200°C to 1370°C, with an accuracy of +/-2.2°C or 0.75% of the measurement.



2.3.3 Turbine RPM measurement

An electromagnetic induction kind of tachometer shown in Fig. 2.5(b) was used to measure the rpm of the compressor. When the generator turbine blades passed the sensor, the sensor would produce a pulse; then the pulse signal would be delivered to the data acquisition system. Using a conversion program, the pulse signal can be transformed to represent the rpm of the compressor.

2.3.4 Fuel pressure measurement

A ball flow meter was installed on the fuel line before the injection in the combustor chamber [Fig. 2.5(c)]. The flow meter was calibrated with an


accuracy of 1% of the full scales.

2.3.5 Fuel flow rate measurement

The fuel supply system is the main component to start the MGT, and the flow rate of the fuel not only needs to be sensed but also to be controlled. A mass flow controller (MFC) is a closed-loop device that sets, measures, and controls the flow of a particular gas or liquid. In this study, a TC-1350 MFC produced by Tokyo Keiso Company was adopted [Fig. 2.5(d)]. The TC-1350 MFC was calibrated to measure and control the methane fuel.

2.4 Test stand operating procedures

Safety Notes

- 
- (1) During operation and for a time afterwards parts of the engine are hot enough to cause serious burns.
 - (2) Always have a fire extinguisher on hand when running; CO₂ or BCF are ideal – dry powder, foam or water are not recommended.
 - (3) This engine must not be used near flammable gases, liquid or materials.
 - (4) Keep all spectators away from the side and rear of the engine to a distance of at least 10M radius, as shown. If operating from a pit area, take special care as safety distance is often difficult to maintain.
 - (5) Maximum exhaust temperature is 800°C and should not be altered.

Turning on the MGT:

- (1) Connect the blower to the MGT air inlet using the rubber tube and connect the fuel pipe.

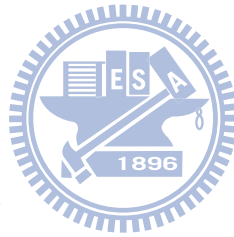
- (2) Connect the lubricating oil pipe. The oil pump is used to fill the pipe with lubricating oil, ensuring that no air enters the pipe as air would plug the pipe and stop the pump. Then, connect the spark plug to the power supply and ensure that the spark plug ignites.
- (3) Set up all measure sensors for RPM, temperature, pressure, flow rate and power output, and connect these sensors to the data Acquisition device.
- (4) Use propane to ignite the MGT, and then change the liquid fuel to a fuel with a low-heating value. Turn on the valves of both of the bottles, and apply the appropriate pressure for each fuel.
- (5) When MGT is ignited, quickly switch the three-way valve to let in the low-heating value fuel; simultaneously increase the fuel pressure and the blower flow rate slowly. If MGT stalls, then turn off the flow valve, apply a higher pressure to the low-heating value fuel and redo step 4.
- (6) Turn on the lubrication pump. Carefully measure temperature, and maintain temperature $< 500^{\circ}\text{C}$.
- (7) When the MGT reaches 40000RPM, the blower and rubber tube can be removed.
- (8) Adjust the rotation rate to 40000-80000RPM, and measure power outputs (voltage and current), temperature, pressures and flow rate.

Shutdown the MGT:

- (1) Slowly turn off the flow rate control valve and lubrication pump.
- (2) Connect the blower to the MGT air inlet via the rubber tube, and use the air sucked by the blower to cool the MGT to 50°C .
- (3) Turn off valves on fuel supply the bottles.

2.5 Parameters of tests

The parameters of the tests included fuel concentration (the mixing ratio of CH_4 and CO_2) and rotation speed of the turbine. The fuel mixtures contained 90% CH_4 with 10% CO_2 , 80% CH_4 with 20% CO_2 , 70% CH_4 with 30% CO_2 , 60% CH_4 with 40% CO_2 and 50% CH_4 with 50% CO_2 . In the experiments, stable RPM, 45,000 RPM, was reached. At each assigned time step, RPM was gently increased by a value of 5000 RPM. After the MGT was stabilized, then held the specific RPM and the engine would be maintained in this stable condition for 10 seconds to measure the data. The experiments were tested with six different fuels, and then each fuel was tested to confirm its maximum rotation speed. Each experimental condition was held at least twice for data consistency.



2.6 Uncertainty Analysis

The accuracy of the experimental data should be confirmed before the analyses of experimental results are carried out because the exactitude of the data may not be very good. Uncertainty analysis (or error analysis) is a procedure used to quantify data validity and accuracy [39]. Experimental measuring results are always in errors. Experimental errors can be classified into fixed (systematic) error and random (non-repeatability) error respectively [39]. Fixed error is the same for each reading and can be removed by proper calibration and correction. Random error is different for every reading and hence cannot be removed. The objective of uncertainty analysis is to estimate the probable random error in experimental results.

Reliable estimation can be primarily categorized into single-sample and

multi-sample experiments. If experiments can be repeated enough times by enough observers and diverse instruments, the reliability of the results can be assured by the use of statistics [40]. Such repetitive experiments are called multi-sample experiments. Relatively, when uncertainties are not found by repetition because of time and costs, this would be called single-sample experiments.

2.6.1 The Asymmetric Uncertainties of Thermocouple

Room temperatures are measured by a 1mm diameter K-typed thermocouple, whose signals are sent to a PC-record. The accuracy of the thermocouple itself without coating is $\pm 0.2\%$. Due to the effects of conduction, convection, and radiation, it is worthwhile to check the correctness of gas temperature measured by such K-typed thermocouple. Via an application of energy balance, i.e.,

Energy in = Energy out, or

Convection to the junction of thermocouple = Radiation from the junction of thermocouple + Conduction loss from the probe

Because of the fine thermocouple (1mm), the conduction term can be neglected. Then, the steady-state energy equation can be rewritten as follows.

$$A_w h(T_g - T_t) - A_w \sigma(\varepsilon T_t^4 - \alpha T_w^4) = 0 \quad (2.1)$$

In practice, the flame temperature is much higher than the wall temperature of thermocouple, so the absorption term, αT_w^4 , from the relatively low wall temperature of thermocouple can be removed from Eq. (2.1). According to Eq. (2.2), the expression of correlation is given as:

$$T_g = T_t + \frac{\varepsilon \sigma T_t^4}{h} \quad (2.2)$$

where T_g = the true gas temperature

T_t = the temperature measured by thermocouple probe

ε = emissivity of the thermocouple

σ = Stefan Boltzmann constant

h = convection heat transfer coefficient at thermocouple wire surface

Now, the analysis method of uncertainty can be utilized to obtain the uncertainty in the flame temperature from the correlation associated with h , T_t , and ε . The relationship between temperature and error is shown in Fig. 2.6.

2.6.2 Uncertainty Analysis of mass flow controller

The apparatuses must be corrected by other standard instruments to make sure that they can normally operate and let the inaccuracy of the experimental results reduce to minimum. In this study, the major sensor in the experiment was the mass flow controller (MFC). The measurement range of the TC-1350 MFC adopted in this study was 0.6-100L/min \pm 0.2%. The author also used different type of MFC, series TC-3100, which had wider measurement range as the standard correction apparatus to correct the TC-1350 MFC. All the uncertainties in different flow rate were between -0.05% and 0.12%.

2.6.3 The Experimental Repeatability

To verify experimental accuracy, perform one test using the specified mixed fuel at the specified pressure and flow rate; perform each test three times to ensure experimental repeatability. The following examples demonstrate experimental repeatability. The volume flow rates for four fuels with LHVs and

RPMs are chosen to demonstrate experimental repeatability. The evaluation included three measurements for volume flow rate; the average value for each test was used. Standard deviation is defined as the absolute difference among the three volume flow rates. Table 2.2 and Fig. 2.7 show the coefficients of variation (CV) and experimental error bars. The CV is defined as the ratio of standard deviation s to mean \bar{X} , where s is derived by

$$s = \sqrt{\frac{1}{N} \sum_{i=1}^N (X_i - \bar{X})^2} \quad (2.3)$$

The CV is a dimensionless number that can be used to specify the variation of data points in a data series around the mean. As the experiments were conducted outdoors, environmental conditions were difficult to control, for safety reason. As a consequence, the errors (<3%) in these experiments were expected to be higher than general experiment errors, but they should be acceptable. Experimental repeatability was apparently very high (Table 2.2).

Table 2.2: Experimental repeatability for volume flow rate for various fuels.

60% Methane						
RPM	1st(L/min)	2nd(L/min)	3rd(L/min)	average	s	CV(%)
40000	45.9382	45.6556	44.3682	45.32	0.68	1.51
42000	48.5758	49.5492	48.2461	48.79	0.55	1.13
45000	51.1349	52.752	54.5575	52.81	1.40	2.65
46000	53.4271	54.3377	55.421	54.40	0.82	1.50
47500	55.3582	55.6879	57.5562	56.20	0.97	1.72
70% Methane						
RPM	1st(L/min)	2nd(L/min)	3rd(L/min)	average	S	CV
45000	42.0912	41.9728	40.8332	41.63	0.57	1.36
50000	46.8568	47.9964	44.8588	46.57	1.30	2.78
55000	51.874	51.2672	51.2228	51.45	0.30	0.58
60000	54.7452	51.4448	54.1828	53.46	1.44	2.70
80% Methane						
RPM	1st(L/min)	2nd(L/min)	3rd(L/min)	average	S	CV
45000	35.0908	35.7124	35.3572	35.39	0.25	0.72
50000	38.8056	40.3004	39.9304	39.68	0.64	1.60
55000	43.1568	42.7276	44.2372	43.37	0.64	1.46
60000	46.4572	46.1612	47.4044	46.67	0.53	1.14
65000	51.9036	51.2376	51.3412	51.49	0.29	0.57
70000	55.87	53.8276	55.8848	55.19	0.97	1.75
75000	57.65	58.33	55.32	58.10	0.97	1.75
90% Methane						
RPM	1st(L/min)	2nd(L/min)	3rd(L/min)	average	s	CV
45000	31.5388	31.302	30.906	31.25	0.26	0.84
50000	35.3128	35.2536	34.1955	34.92	0.51	1.47
55000	39.6788	38.6724	37.3473	38.57	0.95	2.48
60000	43.3344	42.5796	40.545	42.15	1.18	2.80
65000	47.138	46.4276	44.4006	45.99	1.16	2.52
70000	49.9056	50.246	47.6748	49.28	1.14	2.31
75000	54.094	53.9608	51.7905	53.28	1.06	1.98
80000	57.5128	57.3944	55.5237	56.81	0.91	1.60
85000	58.904	58.3268	59.9607	59.06	0.68	1.15

Chapter 3

Numerical analyses

3.1 Domain descriptions

The domain of combustion chamber consists of three major components. They are the solid annulus dual liners (inner and outer), which have several discharge holes, the vaporizing tube, which plays the role of fuel transportation, and the fluids, such as gas fuel and air, filling with the remaining spaces. The annulus combustor has twelve fuel tubes and the liner holes and relative components are in a periodic arrangement shown as Fig 3.1(a) and (b). Therefore, the combustor can be divided into one-twenty fourth sub-chambers geometrically as shown in Fig 3.1(c) and (d), which also represent the configuration of the full-size, three dimensional model domain employed for simulation. The components configuration of sub-chambers is shown as Fig. 3.2, and the size specification of sub-chamber is shown as Fig. 3.3.

3.2 Governing equations

In order to make the physical problem more tractable, several assumptions are made as follows:

1. One-twenty fourth annular zone of actual physical domain is considered due to symmetry, as shown in Fig. 3.1(c).
2. All gaseous mixtures are regarded as the ideal gases.
3. The flow is steady, compressible, and turbulent.
4. Properties in solid are constant.
5. Neglect the turbulence-combustion interaction and radiation heat transfer.

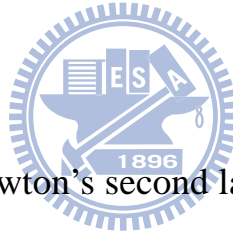
6. One step global reaction is adopted to represent the chemical reaction of methane gas combustion.
7. Soret (or thermo) diffusion, accounting for the mass diffusion resulting from temperature gradients, is neglected [41].

Based on the assumptions mentioned above, the governing equations are given as follows [42]:

Mass conservation:

$$\nabla \cdot (\rho \vec{V}) = 0 \quad (3.1)$$

which describes the net mass flow across the control volume's boundaries is zero.



Momentum conservation:

Based on the general Newton's second law and particular viscous stress law, the momentum equations are developed as Navier-Stokes equations:

$$\frac{\partial}{\partial x_j} (\rho u_j u_i - \tau_{ij}) = -\frac{\partial p}{\partial x_i} \quad (3.2)$$

where suffixes i , and j represent Cartesian coordinates ($i = 1,2,3$), u_i and u_j are absolute fluid velocity components in directions of x_i and x_j , ρ is density, τ_{ij} is shear stress tensor component, and p is pressure.

In Newtonian fluid, the viscous stresses are proportional to the deformation rates of the fluid element. The nine viscous stress components can be related to velocity gradients to produce the following shear stress terms:

$$\tau_{ij} = 2\mu s_{ij} - \frac{2}{3}\mu \frac{\partial u_k}{\partial x_k} \delta_{ij} - \overline{\rho u_i u_j} \quad (3.3)$$

$$s_{ij} = \frac{1}{2} \left(\frac{\partial u_i}{\partial x_j} + \frac{\partial u_j}{\partial x_i} \right), \quad (3.4)$$

where μ is the molecular dynamic fluid viscosity, δ_{ij} the 'kronecker delta', which is unity when $i = j$ and zero otherwise, s_{ij} the rate of strain tensor.

For turbulent flow, u_i , p and other dependent variables, including τ_{ij} , assume their ensemble averaged values. Get back to Eq. 3.3, the rightmost term represents the additional Reynolds stresses due to turbulent motion. These are linked to the mean velocity field via the turbulence models. u' is fluctuation about the ensemble average velocity and the overbar denotes the ensemble averaging process.

Energy conservation:

Heat transfer processes are computed by energy equation in the form known as the total enthalpy equation:

$$\nabla \cdot (\rho u_i h) = \nabla \cdot (k_{eff} \nabla T) + \frac{\partial}{\partial x_j} (u_i \tau_{ij}) + S_h \quad (3.5)$$

where S_h are the energy sources, h is the total enthalpy and defined as:

$$h = i + \frac{p}{\rho} + \frac{1}{2} (u^2 + v^2 + w^2) \quad (3.6)$$

where i is internal energy. k_{eff} is the effective thermal conductivity of the material. In laminar flow, this will be the thermal conductivity of the fluid, k ; In turbulent flow,

$$k_{eff} = k + \frac{\mu_t C_p}{Pr_t} \quad (3.7)$$

where Pr_t is the turbulent Prandtl number.

Species conservation:

$$\frac{\partial}{\partial x_j}(\rho u_j Y_i) = \frac{\partial}{\partial x_j} \left(\rho D_i \frac{\partial Y_i}{\partial x_j} \right) + M_i \omega_i \quad (3.8)$$

where Y_i represents mass fraction for mixture gas of CH_4 , O_2 , CO_2 , H_2O and inert N_2 . The term $M_i \omega_i$ is mass production rate of species. M_i is the molecular weight of i-th species. ω is global one-step reaction rate and in the Arrhenius form for methane combustion is computed as [43]:

$$\omega = k_r Y_{CH_4} Y_{O_2} \quad (3.9)$$

where k is the reaction rate constant for methane combustion reaction:

Here four-step global reaction mechanism is adopted, the pre-exponential factor, temperature exponent and activation temperature are described as follows:

(1) Four-step global reaction mechanism



with the reaction rate expression as [43]:

$$d[CH_4] = -(4.4 \times 10^{11}) e^{\left(\frac{-15105.7}{T}\right)} [CH_4]^{0.5} [O_2]^{\frac{5}{4}}$$

$$d[CH_4] = -(3.0 \times 10^{08}) e^{\left(\frac{-15105.7}{T}\right)} [CH_4][H_2O]$$

$$d[CH_4] = -(2.5 \times 10^{16}) e^{\left(\frac{-20141}{T}\right)} [H_2]^{0.5} [O_2]^{\frac{9}{4}} [H_2O]^{-1}$$

$$d[CH_4] = -(2.75 \times 10^{09}) e^{\left(\frac{-10070.5}{T}\right)} [CO][H_2O]$$

The dynamic viscosity for each species is calculated using Sutherland's law [44]:

$$\mu = \frac{aT^{\frac{3}{2}}}{(b+T)} \quad (3.14)$$

where a and b are constants, they are specific for different species. The selected values for species which we need are tabulated in Table 3.1.

The mean specific heat at constant pressure, C_p , can be written as

$$C_p = \sum_{i=1}^N C_{p_i} Y_i \quad (3.15)$$

JANNAF thermodynamic polynomials are used to estimate the specific enthalpy, h_i , and specific heat, C_{p_i} , for each species; [45]

$$\frac{C_{p_i}}{R} = a_{1,i} + a_{2,i}T + a_{3,i}T^2 + a_{4,i}T^3 + a_{5,i}T^4 \quad (3.16)$$

$$\frac{h_i}{RT} = a_{1,i} + \frac{a_{2,i}T}{2} + \frac{a_{3,i}T^2}{3} + \frac{a_{4,i}T^3}{4} + \frac{a_{5,i}T^4}{5} + \frac{a_6}{T} \quad (3.17)$$

The coefficients, $a_{1,i}$, $a_{2,i}$, $a_{3,i}$, $a_{4,i}$, $a_{5,i}$, and $a_{6,i}$ in Eqs. (3.16) and (3.17) can be found in Table 3.2.

Gas thermal conductivity, k , is derived from Prandtl number:

$$Pr = \frac{\mu C_p}{k} \quad (3.18)$$

in this work, $Pr=0.707$ is selected.

The diffusion coefficient, D , is calculated by Schmidt number:

$$Sc = \frac{\mu}{D} \quad (3.19)$$

in this work, $Sc=0.7$ is selected. The constant properties of solid are tabulate in Table 3.3. [46]

Turbulent model

The Reynolds averaged Navier-Stokes simulation adopt $k - \varepsilon$ model which involves solutions of transport equations for turbulent kinetic energy and its rate of dissipation. The model adopted here is based on Launder and Spalding (1974). In the model, the turbulent viscosity is expressed as:

$$\nu_t = \frac{C_\mu k^2}{\varepsilon} \quad (3.20)$$

the transport equation for k and ε are,

$$\frac{\partial}{\partial x_j} (\rho u_j k) = \rho P - \rho \varepsilon + \frac{\partial}{\partial x_j} \left[\left(\mu + \frac{\mu_t}{\sigma_k} \right) \frac{\partial k}{\partial x_j} \right] \quad (3.21)$$

$$\frac{\partial}{\partial x_j} (\rho u_j \varepsilon) = C_{\varepsilon_1} \frac{\rho P \varepsilon}{k} - C_{\varepsilon_2} \frac{\rho \varepsilon^2}{k} + \frac{\partial}{\partial x_j} \left[\left(\mu + \frac{\mu_t}{\sigma_\varepsilon} \right) \frac{\partial \varepsilon}{\partial x_j} \right] \quad (3.22)$$

with the production term P defined as:

$$P = \nu_t \left(\frac{\partial u_i}{\partial u_j} + \frac{\partial u_j}{\partial x_i} - \frac{2}{3} \frac{\partial u_m}{\partial x_m} \delta_{ij} \right) \frac{\partial u_i}{\partial x_j} - \frac{2}{3} k \frac{\partial u_m}{\partial x_m} \quad (3.23)$$

the five constants used in this model are [36]:

$$C_\mu = 0.09, \quad C_{\varepsilon_1} = 1.44, \quad C_{\varepsilon_2} = 1.92, \quad \sigma_k = 1.0, \quad \sigma_\varepsilon = 1.3$$

the standard $k - \varepsilon$ model is a high Reynolds model and is not intended to be used in the near-wall regions where viscous effects dominate the effects of turbulence. Instead, wall functions are used in cells adjacent to walls. Adjacent to a wall the non-dimensional wall parallel velocity is obtained from

$$u^+ = y^+ \quad u^+ \leq y_v^+ \quad (3.24)$$

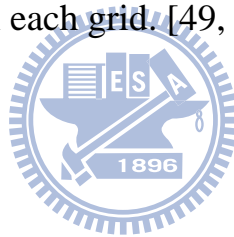
$$u^+ = \frac{1}{\kappa} \ln(Ey^+) \quad y^+ > y_v^+ \quad (3.25)$$

where:

$y^+ = y \frac{u_\tau}{\nu}$, $u^+ = \frac{u}{u_\tau}$ ($u_\tau = C_\mu^{1/4} k^{1/2}$ and $\kappa = 0.4$), and $E = 9.0$ for smooth walls [36].

3.3 CFD-ACE+ software

This work uses a commercial package software, CFD-ACE+, to carry out the numerical computation. CFD-ACE+ is an Advanced CFD and Multiphysics software for simulations of fluid, thermal, chemical, biological, electrical and mechanical phenomena [47]. The solver, based on a finite-volume method [48], divides the physical domain into many control volumes invoked by computational grids and then discretizes differential equation into algebraic one for numerical computation on each grid. [49, 50]



3.4 Numerical method

The CFD-ACE+ employs the finite-volume method to discretize the partial differential equations and then utilize SIMPLEC scheme to obtain the pressure and velocity fields by solving mass and momentum conservation equations. Then, substitute the obtained pressure and velocity fields into energy, species equations, etc. in sequence.

3.5 Boundary conditions

In the model domain, it consists of two inlets, one outlet, two physical symmetric surfaces (including one cyclic symmetric surface), interfaces between two different phases (solid and gas), and the remaining wall. The non-slip boundary conditions are applied on the solid walls. The outlet locates at the rear

of combustion chamber whose function is to guide the hot gas to generate thrust power. The outlet conditions of combustion chamber mainly determined by what is happened upstream. The parameters, such as temperature, velocity, and pressure, at outlet boundary are assumed zero gradients there, and the flow rate in outlet boundary must satisfy with mass balance. The air and fuel inlet boundary conditions are summarized in Table 3.4.

What follows give an example involved the calculation methods and steps for setting of boundary conditions.

Operating conditions:

The compressor wheel works at the rotational speed 80000 rpm, and compression ratio (CR) 1.35.

3.5.1. The inlet boundary conditions

There are two inlet boundaries. One supplied compressed air from the end of diffuser, and the other one supplied mixed fuel gas.

3.5.1.1 Air inlet boundary conditions of combustor

The boundary conditions here are demanded for temperature, velocity, turbulent kinetic energy, turbulent dissipation rate, and spicity mass fraction.

Step1. Modified compression ratio:

The user manual of MGT MW54 accounts for the compression ratio of compressor produced by Garrett is needed to be modified when it is assembled on this engine type. The empirical formula of modified compression ratio is

$$\pi_{\text{mod.}} = \sqrt{\pi}, \quad \pi = \text{compression ratio} \equiv \frac{\text{Outlet pressure of the compressor}}{\text{Inlet pressure of the compressor}} \quad (3.26)$$

$$\Rightarrow \pi_{\text{mod.}} = \sqrt{1.35} = 1.162$$

Step2. Look up the corresponding values for mass flow rates \dot{m} and compression efficiency η at the specified operating conditions on compressor map for a rotational speed 80000 rpm, and compression ratio 1.35.

$$\begin{aligned} \Rightarrow \eta &= 0.7 \\ \dot{m} &= 0.1059(\text{kg} / \text{s}) \end{aligned} \quad (3.27)$$

Step3. Decide the temperature rises after compressing process:

The temperature after compressor was decided by experimental data.

$$\begin{aligned} T_1 &= 295.08\text{K} \\ T_2 &= 326\text{K} \end{aligned} \quad (3.28)$$

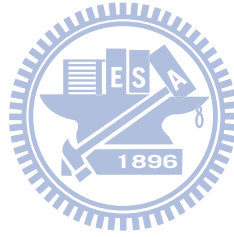
Step4. Calculate the air flow speed velocity at compressor outlet:

According to state equation and continuity equation, the air flow velocity for outlet of compressor is derived as

$$P_2 = \pi_{\text{mod}} \cdot P_1 = \rho RT \quad (3.29)$$

$$\Rightarrow \rho = 1.25 \left(\frac{\text{kg}}{\text{m}^3} \right)$$

$$\dot{m}_{\text{air}} = \rho VA \quad (3.30)$$



where A is the outlet cross-section of compressor

$$\Rightarrow 0.1059 \left(\frac{\text{kg}}{\text{s}} \right) = 1.25 \left(\frac{\text{kg}}{\text{m}^3} \right) \times V \times 1545.66(\text{mm}^2), \quad V = 54.8 \left(\frac{\text{m}}{\text{s}} \right)$$

Step5. Decide turbulent kinetic energy and dissipation rate

Set turbulence intensity by empirical formula [48]:

$$\begin{aligned} I &= 0.16 \text{Re}^{-\frac{1}{8}} \\ \Rightarrow \text{Re} &= \frac{\rho V D_h}{\mu} = \frac{1.25 \left(\frac{\text{kg}}{\text{m}^3} \right) \times 54.8 \left(\frac{\text{m}}{\text{s}} \right) \times 12(\text{mm})}{0.00001956(\text{kg} / \text{s} \cdot \text{m})} = 42033.4(\text{turbulent flow}) \end{aligned} \quad (3.31)$$

where D_h is the hydraulic diameter of compressor outlet

$$\Rightarrow I = 0.04$$

Set dissipation rate in terms of hydraulic diameter:

$$\Rightarrow D_h = 12(mm)$$

Step6. Set species compositions and mass fraction of air at compressor outlet

Mass fraction: $N_2 = 0.768$, $O_2 = 0.232$

3.5.1.2 Fuel inlet boundary conditions of combustor

The boundary conditions here are demanded for temperature, mass flow rate, turbulent kinetic energy, turbulent dissipation rate, and species mass fraction.

Step1. The volume flow rate of the fuel

Total fuel consumption is $56.8(L/min)$ at $P = 10.083bar$.

Step2. Set species compositions of mixed fuel at fuel tube inlet

Set different ratio CO_2 gas mixed with methane. For example, volume percentage as 90% methane, 10% CO_2 possess mixed molecular weight:

$$90\% \times 16 + 10\% \times 44 = 14.4 + 4.4 = 18.8$$

$$\therefore \text{mass fraction of } CH_4 = \frac{14.4}{18.8} = 0.766$$

$$\text{mass fraction of } CO_2 = 0.234$$

Step3. Set boundary temperature $T_{ambient} = 298K$

Step4. Set turbulence intensity $I = 0.0564$, dissipation rate in terms of hydraulic diameter $D_h = 0.001(mm)$.

Because the practical operating conditions of the compressor could afford range from critical rotating speed 80000 rpm to idle 45000 rpm according to compressor map, in addition to implement the case of operating condition 80000 rpm to simulate, the study provides the other three operating conditions of rpm 70000, 60000, and 50000 to simulate.

3.5.2 The outlet boundary conditions

The only one outlet locates at the rear of combustor chamber whose function is to exhaust the hot gas to generate thrust power. The outlet conditions of combustion chamber are mainly determined by what is happening upstream. The pressure at outlet boundary is defined as casing pressure P_2 which is derived from Eq. (3.29). The parameters such as temperature, velocity, pressure, at outlet boundary are assumed zero gradients, and the flow rate in outlet boundary must satisfy with mass balance.

3.5.3 The symmetry boundary conditions

The component of velocity vector which perpendicular to symmetric surfaces are set zero.

3.5.4 The interface boundary conditions

The interfaces between two different phases, solid and gas, are the no-slip boundary conditions ($u, v, w = 0$).

3.5.5 Wall boundary conditions

Except the inlet, outlet, symmetry, and interface boundaries, the remaining geometry is all wall boundaries, which are the no-slip boundary conditions ($u, v, w = 0$) for velocity and adiabatic for temperature.

3.6 Computational procedure of simulation

In solving the Navier-Stoke Equations, the Semi-Implicit Pressure Linked Equation Correlation (SIMPLEC) algorithm was a widely used numerical method. Different from other algorithms adopting finite difference method, this

SIMPLEC adopted finite volume method. Figure 3.4 (a) shows the model of annular combustion chamber used in the CFD-ACE+. It was developed by Solid-Works; then, imported to the CFD-ACE+ as IGS file. Afterwards, the mesh arrangement was accomplished and shown in Figure 3.4 (b) by the CFD-ACE+ pre-processing, also called CFD-GEOM.

3.7 Grid-independence test

For obtaining the acceptable numerical solution, this study applied the unstructured grids produced from geometry models to carry out grid-independence test. The grid-independence test comprised combustion case. Because the over-heating problem of liners is one of concerns in this research, the grid densities is increased especially near the liners, whose thicknesses are only 0.4mm, and the fuel tube, which is about 0.5mm in thickness. Owing to adoption of upwind numerical difference scheme, the grid amount should be dense enough to avoid the false diffusion phenomenon.

For grid test, the operating conditions are specified as that the air inflow of $\dot{m}=0.0044$ kg/s is generated by compressor with a compression ratio 1.35 under the rotation rate 80000 rpm, and the fuel tube supplies a mixing fuel of methane (mass fraction 0.766) and CO₂ (mass fraction 0.234) under a fixed mass flow rate ($\dot{m}=3.325E-05$ kg/s). From the above discussion, the mass flow rate, velocity and temperature of gas mixture ejected from the rear of combustion chamber are the emphasized data

The grid numbers adopted for the grid-independence tests in this case are 477181, 717974, and 1484378. The test results are listed in Table 3.5. From the information given by the table, it can be seen that the maximum relative errors

of various physical quantities are all less than 3%. Under such circumstance, it is naturally to select the grid number of 477181 to compromise the computational time. Pentium 4 with CPU 3.0 GHz, 2GB RAM is used to carry out the computation, and select convergence criterion as 10^{-3} . Then the computational time for a typical simulation in the c case needs about 60 hours.

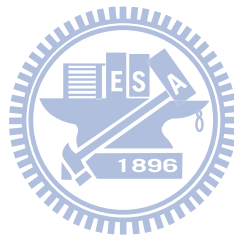


Table 3.1: Sutherland's law coefficients of dynamic viscosity

Sutherland's Law Coefficients	Species							
	CH4	O2	CO2	H2O	CO	H2	H	N2
A	1.25E-06	1.78E-06	1.50E-06	1.86E-06	1.50E-006	6.89E-007	6.89E-007	1.40E-06
B	197.4	156	222.26	708	136.35	96.69	96.69	111.5

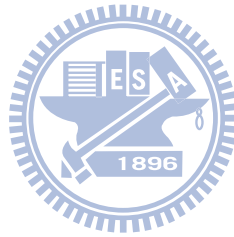


Table 3.2: JANNAF coefficients of gas specific heat

	Species							
Temperature limits(K)	CH ₄	O ₂	CO ₂	H ₂ O	CO	H ₂	H	N ₂
lower limit	300							
break point	1000							
upper limit	5000							
Coefficients at lower limit	※ These coefficients will be used at temperatures between the lower limit and the break point							
a1	7.79E-01	3.21E+00	2.28E+00	3.39E+00	3.26E+00	3.30E+03	2.5	3.30E+00
a2	1.75E-02	1.13E-03	9.92E-03	3.47E-03	0.15E-02	0.82E-03	0	1.41E-03
a3	-2.78E-05	-5.76E-07	-1.04E-05	-6.35E-06	-3.88E-006	-8.14E-07	0	-3.96E-06
a4	3.05E-08	1.31E-09	6.87E-09	6.97E-09	5.58E-09	-9.48E-11	0	5.64E-09
a5	-1.22E-11	-8.77E-13	-2.12E-12	-2.51E-12	-2.47E-12	4.13E-13	0	-2.44E-12
a6	-9.83E+03	-1.01E+03	-4.84E+04	-3.02E+04	-1.43E+04	-1.01E+03	2.55E+04	-1.02E+03
a7	1.37E+01	6.03E+00	1.02E+01	2.59E+00	4.85E+00	-3.29E+00	-0.46E+00	3.95E+00
Coefficients at upper limit	※ These coefficients will be used at temperatures between the break point and the upper limit							
a1	1.68E+00	3.70E+00	4.45E+00	2.67E+00	3.02E+00	2.99 E+00	2.5	2.93E+00
a2	1.02E-02	6.14E-04	3.14E-03	3.06E-03	0.14E-02	0.70E-03	0	1.49E-03
a3	-3.88E-06	-1.26E-07	-1.28E-06	-8.73E-07	-5.63E-07	-5.63E-08	0	-5.68E-07
a4	6.79E-10	1.78E-11	2.39E-10	1.20E-10	1.02E-10	-9.23E-12	0	1.01E-10
a5	-4.50E-14	-1.14E-15	-1.67E-14	-6.39E-15	-6.91E-15	1.58E-15	0	-6.75E-15
a6	-1.01E+04	-1.23E+03	-4.90E+04	-2.99E+04	-1.43+04	-8.35E+02	2.55E+04	-9.23E+02
a7	9.62E+00	3.19E+00	-9.55E-01	6.86E+00	6.11E+00	-1.36E+00	-0.46E+00	5.98E+00

Table 3.3: Properties of solid liner

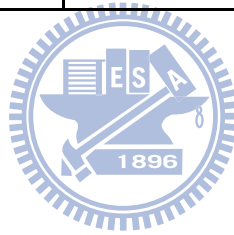
Material	Density(kg/m ³)	Specific heat(J/kg-K)	Thermal conductivity(W/m-K)
Steel_AISI_1020	7900	470	48

Table 3.4: Boundary conditions of combustion chamber

Conditions	Air Inlet			Fuel Inlet			
				60% Methane	70% Methane	80% Methane	90% Methane
	Hydraulic diameter(D_h)=0.012 m			D_h =0.01 m	D_h =0.01 m	D_h =0.01 m	D_h =0.01 m
	Turbulence intensity (I)=0.04			I =0.04	I =0.04	I =0.04	I =0.04
	$Y_{N_2}=0.768$ $Y_{O_2}=0.232$			$Y_{CH_4}=0.353$	$Y_{CH_4}=0.459$	$Y_{CH_4}=0.593$	$Y_{CH_4}=0.766$
				$Y_{CO_2}=0.0647$	$Y_{CO_2}=0.541$	$Y_{CO_2}=0.407$	$Y_{CO_2}=0.234$
				T=297K	T=296K	T=295K	T=295K
R.P.M	CR	\dot{m} (kg/s)	T2(K)	Flow velocity of fuel(m/s)			
40000	1.050	0.001575	306.0	80.14			
42000	1.063	0.001654	306.7	86.28			
45000	1.081	0.001765	307.8	94.80	73.60	62.58	55.30
46000	1.088	0.001800	308.5	96.20			
47500	1.100	0.001890	308.9	99.00			
50000	1.140	0.002040	309.0		82.36	70.17	61.75
55000	1.145	0.002360	310.5		91.00	76.70	68.20
60000	1.182	0.002500	313.0		95.50	82.53	74.57
65000	1.209	0.002680	315.89			91.00	81.33
70000	1.245	0.003300	318.80			97.60	87.00
75000	1.294	0.004100	322.69			102.60	94.20
80000	1.355	0.004400	326.19				100.00
85000	1.400	0.004700	332.50				104.00

Table 3.5: Grid test results of different grid densities for numerical simulation

	477181 grids	717974 grids	1484378 grids	Maximum Relative Error (%)
Outlet mass flow rates (kg/s)	4.18×10^{-3}	4.17×10^{-3}	4.25×10^{-3}	1.9
Outlet max. temperature (K)	645	641	655.2	2.2
Outlet max. velocity (z-direction) (m/s)	108.9	106	106.4	2.3
Average outlet velocity (z-direction) (m/s)	80.6	81.5	82.9	2.5



Chapter 4

Dynamic Model of MGT for Control Strategy

This section describes the development of a dynamic model for the proposed MGT system. According to the thermal process of the MGT, different models have been developed to predict the dynamic response behaviors of gas turbine systems. The MGT's dynamic model used in this study is adapted from that developed by Rowen [51]. This model is commonly used due to its simplicity and flexibility in adjusting to turbines with different characteristics.

An outline of the structure, including the control and fuel systems, was generated using Matlab/Simulink (Fig. 4.1); the relevant equations are

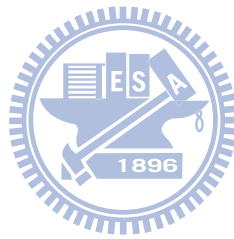
$$F_1 : \\ T_x = \frac{Tr - y \times [1 - (V_{fuel} - 0.4)] \times (N^2 - 4.21 \times N + 4.42) + z(1 - N)}{1 + 0.005(22 - T_{amb})} \quad (4.1)$$

$$F_2 : \\ Torque = k_{HHV} \times (V_{fuel} - 0.4) + a \times (1 - N) \quad (4.2)$$

where k_{HHV} is the high heating value (HHV) factor, V_{fuel} is the volume flow rate of the fuel, T_{amb} is ambient temperature, Tr is the maximum exhaust temperature, T_x is predicted exhaust temperature, $Torque$ is predicted mechanic torque produced by the MGT, a , y and z are correlation factors, and N (p.u) is compressor rotational speed. These equations can calculate turbine torque and exhaust temperature algebraically.

Signal V_{fuel} , which represent the volume flow rate of fuel, is the most

important variable when operating the MGT. In numerical simulation of the dynamic model of the MGT, compressor rotational speed, exhaust temperature of the MGT, and MGT loading were functions of V_{fuel} . Notably, V_{fuel} was utilized to calculate MGT mechanic torque and exhaust temperature after the simulation signal was modulated by a time delay block generated by combustion reactions.



Chapter 5

Results and Discussions

5.1 Experimental results and discussions

The original MGT, which was powered by liquid fuel, was modified to run on gaseous fuel. Therefore, the original pipes were changed accordingly. Additionally, the lubricant for bearings in the original MGT was pre-mixed with oil fuel. The lubricant supply system was separated from the fuel pipes after modification. In the experiments, stable rotational speed, 45,000 RPM, was reached. To increase fuel efficiency, data were obtained at each step as the rotational speed was increased by 5000 RPM increments. Each step was maintained for approximately 10 seconds to ensure that the engine reached a stable condition such that measured output data at each step were meaningful; otherwise, stop-and-run experiments would consume a substantial amount of gas and the time required would be excessive. Additionally, maximum exhaust temperature was set at 800°C for safety reasons.

5.1.1 Tests using various fuels with no load

The proposed MGT was tested without loading. Various fuels with LHV with various mixture ratios of methane (CH_4) to carbon dioxide (CO_2) were used. The concentrations of CH_4 in the fuel were in the range of 50–90%, and those of CO_2 increased from 10% to 50%. The temperatures of the main components of the MGT were measured at a specified fuel and fuel flow rate against cylinder gauge pressure. Thermal efficiency was calculated accordingly. Finally, the performances of the MGT under the various test conditions were compared.

5.1.1.1 Pressures and volume flow rates of fuel in the MGT

Fuel pressure was the pressure exerted by the cylinder (bottle); this pressure was adjusted using a control valve. Fuel pressure was determined by fuel volume flow rate. The volume flow rate of each fuel was measured as a function of pressure, and calculated from mass flow rate. (CH_4 density is 0.7168 g/L at 0°C , 1 atm) The volume flow rate of each fuel was roughly linearly proportional to fuel pressure. Figure 5.1 plot rotational speeds as functions of volume flow rates for the various fuels with LHV.

In the test using fuel comprised of 90% CH_4 and 10% CO_2 , the rotational rate approached 85,000 RPM as fuel pressure approached a maximum of 12bar. Under the same pressure, a rate of only 47,500 rpm was reached with 60% CH_4 and 40% CO_2 . The condition of 50% methane could not generate power when loading was applied. More specifically, the power of MGT at 40,000 RPM while applying 50% methane fuel was not able to drive the generator. The author present the results of 50% methane here were tending to offer more information for future research interest. Clearly, the combustible fuel concentration in the LHV fuels influenced the performance of MGT. According to Fig. 5.1, as expected, the fuel with the higher heating value performs better because it can supply more energy to MGT. Also, a higher pressure must be applied to the lower heating-value fuel to approach idleness at 45,000 RPM.

Since MGT performance was proportional to the CH_4 concentration in fuel and volume flow rate, increasing volume flow rate increased MGT performance. Furthermore, using a fuel with a LHV in the MGT originally designed for oil fuel may result in choking of both the turbine wheel and fuel supply pipe. This choking can occur in the nozzle throat or in the annulus at the turbine outlet. As rotational speed increases to $>85,000$ rpm, choking may markedly limit the

rotational rate of the turbine wheel because the rotational speed increases as flow rate increases; however, the maximum fuel pressure reached at 85,000 rpm was 12 bar. Therefore, turbine choking did not occur during tests in this study. Compared to the turbine choking, the choking at fuel supply pipe needs more attention. The original pipe which only have 0.5mm diameter was designed to deliver 0.05L liquid fuel per minute at 80,000 rpm. However, the experiment results showed that the volume of the fuel was 58L and the pressure was 12 bar when the maximum power was reached. Thus, in order to avoid choking condition, the fuel supply system should be modified to deliver more volume of fuel so that the pressure will be reduced and the security will be enhanced.

In this investigation, the equivalent ratio was given by



Air: Fuel (CH₄) = 18.125: 1

The air mass flow rate of 321.12 g/min in the primary zone was determined from the compressor map at 45,000 RPM; the fuel mass flow rate was 26.87 g/min. The Air/Fuel ratio (A/F) was 16.7 less than the equivalent ratio of 18.1; however, at 80,000 RPM, the A/F was 22.5, which was greater than the equivalent ratio of 18.1. Therefore, the A/F increased as rotational speed increased from 45,000 to 80,000 RPM.

Since the volume flow rate was proportional to cylinder pressure, the volume flow rate of fuel was given by the following linear regression equation (CH₄ density is 0.7168 g/L at 0°C, 1 atm):

$$\dot{m} = 5.54 + 4.2P_{out} \quad (5.2)$$

The volume flow rates of the fuels with a LHV were then replaced by those of CH₄. Figure 5.2 presents the corresponding results. At a particular compressor

rotational speed, the volume flow rates of CH_4 obtained for different fuels with LHV were almost equal, indicating that combustion was stable in the proposed MGT, even when different fuels were used.

5.1.1.2 Temperature of unloaded MGT

Temperatures were measured at the compressor inlet (T1), compressor outlet (T2), turbine inlet (T3) and turbine outlet (T4). Figures 5.3 (a-d) indicate that the histories of all temperatures and the corresponding rotational speeds for different LHV fuel. The inlet and outlet temperatures (T3 and T4) of the turbine declined as rotational speed increased because as compressor RPM increased, an increased amount of air enters the combustion chamber, and the turbine was cooled by this additional air. Liou and Leong [52], who experimented with a particular MGT using oil fuel, observed the same phenomenon at 40,000–120,000 RPM. However, when this MGT operated at >120,000 RPM, temperature increased as rotational speed increased.

Turbine inlet (T3) and turbine outlet (T4) temperatures varied slightly as the concentration of CH_4 in fuels varied (Figs. 5.3(a) and (b)). This trend could influence thermal efficiency, which was discussed in Section 5.1.4. Additionally, the difference between T3 and T4 varied minimally with the fuel with a LHV because, at a given compressor rotational speed, the amounts of CH_4 burned were the same for all fuels (Fig. 5.2). T3 and T4 were markedly perturbed at the start of operation because the blower and fuel were manually controlled before the MGT reached stability. Thus, a red dash line was added in Fig. 5.3 to separate an unstable duration of the MGT from the stable one. Excessively increasing the air flow rate markedly reduced T3 and T4. However, an excessive fuel flow rate rapidly increased T3 and T4.

Figure 5.4(a) presents the surface (case) conditions of a combustion chamber using oil fuel; Fig. 5.4(b) presents those of a combustion chamber using gaseous fuel. In Fig. 5.4 (b), The surface condition (color changed) on both the primary and intermediate zones of combustion chamber have been affected by high temperature while applying the LHV fuel, whereas such phenomenon was not appeared when using liquid fuel. Clearly, combustion chamber temperature with methane exceeds that with liquid fuel because the combustion chamber was designed to burn liquid fuel. When gaseous fuel was used, the cooling system was inadequate. Moreover, this experimental conclusion can also be deduced that it is easier to burn methane than oil fuel. Based on the schematic view of the MGT system (Fig. 3.2), the fuel pipe in the combustion chamber is close to the liner wall. Thus, the gas fuel should burn immediately after it is ejected from the fuel pipe and the temperature near the liner wall should be higher than using oil fuel. This phenomenon has been predicted from the numerical results of temperature distribution in the combustion chamber; discussed in section 5.2.

5.1.1.3 Thermal efficiency

The thermal efficiency of the proposed MGT system combined with the adiabatic efficiencies of the compressor and turbine were estimated thermodynamically by assuming a typical and simple Brayton cycle. The reason for selecting this simple Brayton cycle is that this equation is suitable for a single-shaft and low compression-ratio gas turbine that is suggested by Sonntag et al. [53]. The efficiency of the air-standard Brayton cycle is

$$\eta_{th} = 1 - \frac{Q_L}{Q_H} = 1 - \frac{C_p(T_4 - T_1)}{C_p(T_3 - T_2)} = 1 - \frac{T_1 \left(\frac{T_4}{T_1} - 1 \right)}{T_2 \left(\frac{T_3}{T_2} - 1 \right)} \quad (5.3)$$

According to Sonntag [53], because the working fluid does not complete a thermodynamic cycle in the MGT, the internal combustion engine operates on a so-called open cycle. However, when analyzing internal-combustion engines, devising closed cycles that closely approximate open cycle is advantageous.

The thermal efficiency of the proposed MGT was derived from the efficiency of the air-standard Brayton cycle in Eq. (5.3). Figure 5.5 shows thermal efficiency versus compressor rotational speed. For the fuels with different concentration of CH₄, efficiency decreased as rotational speed increased. Based on Eq. (5.3), the thermal efficiency was affected by T₄, T₃, and T₂ (compressor outlet temperature); that is, thermal efficiency decreased because the decrease in T₂ was larger than the decrease in T₃ and T₄ at high RPMs. Fuels with lower concentration of methane had more thermal efficiency (Figs. 5.5). Theoretically, thermal efficiency should not increase with the decrease of methane concentration in fuel. The T₃ in the experiment condition of using 60% methane was larger than using 90% methane. This phenomenon could be observed in Figs. 5.3. The inferences was that the pressures and flow rates of fuels with lower concentration of methane were larger than those of fuels with higher concentration, and high inject pressure of fuel could cause major variation to temperature distribution in combustion chamber because the fuel pipe exit was very close to the front wall of chamber.

5.1.2 Testing MGT with generator

In this section, the MGT with a generator was tested; all test parameters were the same as those used in Section 5.1.1. Temperature was measured and the amount of electricity generated by the generator was discussed. All temperatures measured in the MGT with a generator were similar to those of the unloaded MGT. Notably, the MGT does not directly drive the generator; the generator is driven by a gearbox, which has a power turbine driven by high-temperature and high-pressure gas from the MGT. The generator weakly influences MGT performance. Choosing a generator that fits the MGT is extremely important. If the generator power is too high, loading will be excessive, and the MGT cannot then be operated at a suitable range of rotational speed. If the power generated is too low, the load will be too low and optimal performance cannot be obtained. The worst outcome is that the gearbox of the MGT system breaks when the rotational speed limit is exceeded. The power output obtained using 90% CH₄ fuel was roughly 170W, which was the maximum output of the generator, and 70W at 60,000 RPM as 70% CH₄ with 30% CO₂ was used (Fig. 5.6). When a critical limit of 60% CH₄ was used, the power output was extremely low. The output of the MGT was a function of fuel volume flow rate, which, as stated, was proportional to cylinder pressure. As volume flow increased, performance improved. However, excessively narrow fuel pipes limited the volume flow rate in the MGT system. Thus, the achievable volume flow rate did not exceed 58L/min, even when maximum pressure (12bar) was applied to the system. Thus, pressure must not exceed 12bar to prevent pipe breakage in the MGT system.

Additionally, the electric efficiency which calculated from the power output divided by the fuel release heat due to combustion shown in Eq. (5.4) was around 10%, assuming a reversible, adiabatic, steady-state process.

$$\eta_{electric} = \frac{W}{\sum \Delta h_i m_i} \quad (5.4)$$

where $\eta_{electric}$ is electric efficiency, W is actual work of system, h_i is enthalpy to different species and m_i is mass flow rate to different species. This considerable difference was due to the losses from the connected transmission gear box and the bridge rectifier.

5.2 Numerical Simulation results and discussions

The corresponding simulated mass flow rate of fuel could be divided into four mass-fraction conditions, that is, the highest one was 90 percent of methane and the lowest was 60 percent. All the rotation speed conditions were simulated according to the experimental works. Since a series of parametric studies was carried out, a reference case of steady state of methane concentration, 60%, at idle speed of MGT (45000 RPM) was chosen to serve as a detail illustration case [Fig 5.7 (a-d)]. Table 5.1 presented some important data of the simulation results. Figures 5.8 to 5.11 demonstrated the simulation results of 45000 RPM condition while applying different concentration of CH₄.

Figures 5.7(a) and 5.8 show simulation results of temperature distribution on the symmetric plane (0 degree cross-section) in the annular MGT combustor with different concentration of CH₄, which demonstrated that with an appropriate value of air-fuel ratio, the temperature inside annular combustion chamber core reached 2106.7K (Table 5.2). Thus, combustion existed inside the combustion chamber. From the schematic view of MGT system, it can be realized that the fuel pipe in the combustion chamber is close to the liner wall. Thus, the gas fuel ought to burn right after it ejects from the fuel pipe and the

temperature near the front wall of the combustor is expected to be higher. The simulation results shown in Figs. 5.7(a) indicated that the high-temperature zone did concentrate at the front of the combustion chamber. The combustor chamber could be divided into three zones: primary, intermediate, and dilution zones. They were marked according to the position of liner holes shown in Fig. 5.7(a). The other phenomenon shown in Fig. 5.7(a) was that the cool air flows via dilution holes on liners were fully functional. The jet flow, which discharged from dilution holes, cooled down the exhaust gas temperature effectively. The average exhaust temperature of combustor outlet was below the endurance temperature 800°C (1073K). In Fig. 5.8, the high temperature zone was moved toward the outlet of combustor as the methane concentration decreased. It was because that the fuel flow velocity was increased as the methane concentration was lowered that pushes the flame more downward. Furthermore, the more scattering distributed high temperature areas were induced by the lowered methane concentration. Also, the combustor outlet temperature (T_3) was increased due to the downstream-shifted high-temperature zone with the decrease of methane concentration.

The simulation results shown in Figs. 5.7(b) and 5.9 demonstrated the distribution of CH_4 mass fractions in primary zone. It was realized that the inverse fuel injection system could deliver the fuel properly to ensure that the combustion reaction occurred at the front of the combustion chamber. The fuel mixture of CH_4 and CO_2 was injected into a mixing tube, where it mixed with the concurrent air flow from the back of combustor. Then, the premixed fuel/air was exhausted from the mixing tube and immediately met with the air supplied from the hole of liner above to enter the primary zone. In the meantime, air was also supplied via the hole on the bottom surface of liner. Since such hole in the

primary zone was not located on the symmetric plane, it couldn't be observed in these figures. Because the air and fuel were mixed and burn in the primary zone, the mass fraction of CH_4 decreased gradually from fuel tube exit to primary zone. Eventually, the mass fraction of CH_4 was near zero in the intermediate zone due to the strong dilution from air. In Figs 5.9, the CH_4 mass fraction in primary zone was increased with CH_4 concentration raised. Moreover, larger CH_4 mass fraction produces much more severe reaction at interface zero methane mass fraction and mass diffusion zone of methane concentration gradient.

When the function of intermediate holes was discussed, Figs. 5.7 (c) and 5.10 showed the distribution of O_2 mass fraction with different concentration of CH_4 and indicated that large number of compressed air was induced to the combustion chamber via the intermediate holes. Under this condition, combustion would be done more completely and less dissociated product would occur. There were fourteen air inlets in the computational domain, which can be referred in Fig. 3.4 (a). Only four of them were located on the symmetric plane. In Fig. 5.7 (c), each zone has one air inlet, and the last one is behind the fuel tube. At these air discharge holes, their oxygen mass fractions were 0.232 because they come from fresh air. The intense combustion is occurred in primary zone, the oxygen mass fraction is almost zero here. It increases gradually toward the intermediate zone and finally becomes 0.232 in the dilution zone since about 70% of total supply air entering the combustor flows into the two zones via the holes on the liner to dilute and cool the combustion products.

A conventional turbine engine typically had a swirling mechanism that increases recirculation of the flow. Such recirculation could promote fluid mixing and retain the combustion flame. Simulation results (Figs. 5.7(d) and 5.11) demonstrated that although the annular combustion chamber did not have

a swirling generator, the design still could create an appropriate recirculation zone to confine the flame at the chamber center, and prevent the flame expanding to generate a hot spot. In Fig. 5.7(d), the first recirculation in primary zone was called central recirculation zone which was created due to the inlet air to the combustor had gained tangential component. The tangential component could develop a centrifugal force on flow particles to deflect rather than moving in the axial direction. Another recirculation occurs at the above the bottom liner wall between the two air inlets located at the primary and intermediate zones, respectively. It was resulted from two different air flow velocities via the inlets. It also could be observed that the largest velocity occurred at the exit and the maximum and average values were 55.2 and 42.4 m/s, respectively (Table 5.1). The air flow velocities between the liner walls and casting were relatively smaller. The acceleration as air passes the high temperature area of liner was still observed. Also, the flow velocities at the air inlet were quite great because the area change. Additionally, Fig. 5.11 shows the velocity flow field for each specified concentration of methane at 45000 rpm. From Table 5.1, the outlet temperature was increased with a decreased of methane concentration. However, the variation (1065K~980K) was insignificant, so did the local density. Therefore, the variation of average outlet velocity was coherent with that of outlet mass flow rate. In other word, the outlet velocity was increased as the CH₄ concentration decreased.

Figures 12 (a-d) are the curved charts with different methane concentration and different compressor speed. These figures show the influence of compressor speed are more distinct than the methane concentration does to the parameters of the maximum temperature in combustor, the maximum temperature on liner walls, the maximum temperature at combustor outlet, and the outlet maximum

velocity.

Temperature control and limit is the most important issue while operate the MGT. Overheat condition could damage the MGT seriously. The combustor outlet, which was next to turbine, emitted high temperature gas. The critical endurance temperature of exhaust gas was set at 800°C (1073K) [54]. Moreover, the turbine blade is made of Inconel whose allowance temperature is about 1336 ($=1609\text{K}$). Table 5.1 showed the simulation results of temperature at T3 and the maximum temperature on liner walls. When different methane concentration of simulated fuel was employed, all predictions did not exceed the maximum temperature that the turbine wheel can tolerate. Additionally, Table 5.1 also showed the temperature distribution of the combustor liner at maximum reachable speed condition while applying different concentration of CH_4 . A combustor wall made of Inconel must be capable of tolerating high temperatures. The maximum endurance temperature is roughly 1600K ; therefore, all the simulated conditions were not burned out. Since the distributions of CH_4 mass fraction, O_2 mass fraction and velocity in the combustion chamber were unavailable due to the deficiency of experiment facilities in this study, temperature data were the only information that could be made comparison between the numerical predictions and experiment measurements. Figures 5.13 (a-d) demonstrate the results of maximum temperature at turbine inlet (T3) by using the four-step simulation and the experimental data at different methane concentrations. From these figures, the predicted results of four-step mechanisms are more superior than the experimental measurements. In addition, the chemical mechanism used in this study was a reduction one (4-step) that the simplified chemical reactions were expected to be faster than the actual

chemical reactions. Thus, the four-step reaction mechanism over predicted the maximum temperature in combustor outlet with the experimental data is expected. The results showed that, among these simulation conditions, the heat damages to turbine blade were less than those to liners. One of the reasons was that outlet was away from the solid zone of liners and then it suffered less over-heating problem as mentioned maximum previously. The other one was that the cool air flows via dilution holes on liners were fully functional. The jet flow discharged from dilution holes cool down the exhaust gas temperature effectively. When designing a combustion chamber, hot spots must be prevented as they would burn through the combustion chamber and cause the engine to fail.

5.3 Extended studies results



5.3.1 System identification

The dynamic model identification process is prerequisite for controller design research in the near future. All parameters in the dynamic model can be derived using experimental results for MGT performance. In Eq. 4.2, the HHV of the fuels influenced the required volume flow rate for fuel to air. As the HHV of methane fuel is 13255.95kcal/kg, k_{HHV} factor is defining as 13.255 [51]. Correlation factor a can be derived based on experimental results with the conditions of $V_{fuel} = 0$, $Torque = 0$, and $N = 0$ input into Eq. 4.2. The turbine-torque prediction function is then rewritten as $0 = 13.255 \times (0 - 0.4) + a \times (1 - 0)$, and $a = 5.302$ is calculated algebraically. An experimental result for volume flow rate of fuel was input into the dynamic

model to confirm the reliability of proposed numerical simulation model. The simulation results for variations in compressor speed in the dynamic model shows a great consistency with the experiment data (Fig. 5.14). However, simulation and experimental data differ before 100 sec and after 350 sec. In these periods, the MGT was considered unstable; this status is not discussed herein.

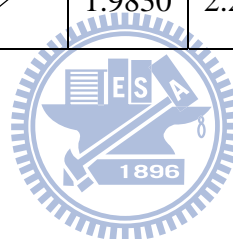
Variations in volume flow rate versus turbine outlet temperature indicate these variables were nonlinearly correlated. In the dynamic model illustrated in Fig. 4.1, Eq. 4.1 in this numerical simulation model should be restricted to represent only the stable status of the MGT system based on experimental results and phenomena. The required inputs for Eq. 4.1 were compressor rotation speed, fuel volume flow rate, and ambient temperature. The effect of ambient pressure on gas turbine output is not addressed herein. Correlation factor y can be calculated using experimental results with the conditions of $V_{fuel} = 0.4$, $T_{amb} = 22$, and $N = 1$ (p.u) input into Eq. 4.1. After correlation factor y was calculated as 20.66, correlation factor z was calculated based on experimental results with the conditions of $V_{fuel} = 0$, $T_{amb} = 22$, and $N = 0$ (p.u); $y = 20.66$ was then input into Eq. 4.1. Correlation factor z was 507.57. The simulation result for the effect of variables, including that of compressor rotation speed, fuel volume flow rate, and ambient temperature, on exhaust temperature were the same as experimental data when the MGT system is in stable status (Fig. 5.15). The completed simulation model will prove to be a helpful base structure when designing an optimal control strategy.

Table 5.1 : Simulation results for four-step reaction mechanism

R. P. M.	42000	45000	46000	47500	50000	55000	60000	65000	70000	75000	80000	85000
	60% Methane											
Maximum temperature in combustor(K)	2106.2	2106.7	2109.0	2112.0								
Maximum temperature on liners(K)	1089.6	1096	1110.0	1117.5								
T3 (K)	1115.5	1065	1053.1	1044.8								
Outlet maximum speed(m/s)	50.6	55.2	56.4	57.4								
Average flow speed of outlet(m/s)	38.9	42.4	43.3	44.1								
Average mass flow rate of outlet(kg/s) $\times 10^{-3}$	1.5907	1.7328	1.7492	1.7961								
	70% Methane											
Maximum temperature in combustor(K)		2108			2125	2133	2142					
Maximum temperature on liners(K)		1119			1130	1169	1207					
T3 (K)		1030.0			1025.5	1017.8	1014.0					

Outlet maximum speed(m/s)	/	50.3	/	/	56.6	64.0	67.6	/	/	/	/	/
Average flow speed of outlet(m/s)	/	39.2	/	/	43.7	49.7	52.3	/	/	/	/	/
Average mass flow rate of outlet(kg/s) $\times 10^{-3}$	/	1.7285	/	/	1.9956	2.3090	2.4448	/	/	/	/	/
	80% Methane											
Maximum temperature in combustor(K)	/	2112.0	/	/	2129.6	2140.0	2152.0	2176.7	2188.7	2233	/	/
Maximum temperature on liners(K)	/	1125.0	/	/	1146.0	1199.0	1230.0	1255.0	1289.0	1310	/	/
T3 (K)	/	999.9	/	/	970.0	955.1	940.5	920.0	909.0	893.0	/	/
Outlet maximum speed(m/s)	/	46.7	/	/	52.9	59.0	65.0	71.5	80.4	91.6	/	/
Average flow speed of outlet(m/s)	/	36.3	/	/	41.0	46.1	50.4	55.2	62.7	72.0	/	/
Average mass flow rate of outlet(kg/s) $\times 10^{-3}$	/	1.7230	/	/	1.9882	2.2987	2.4376	2.6122	3.2178	4.0007	/	/
	90% Methane											
Maximum temperature in combustor(K)	/	2140	/	/	2153	2159	2162	2180	2198	2253	2254	2258

Maximum temperature on liners(K)		1151			1173	1221	1236	1267	1314	1315	1347	1407
T3 (K)		980.2			968.0	944.3	921.1	905.6	890.7	880.5	873.0	856.3
Outlet max. speed(m/s)		46.2			51.8	59.7	63.9	69.9	79.0	92.0	96.5	102
Average flow speed of outlet(m/s)		35.9			40.2	46.5	49.6	54.1	61.9	72.2	75.7	80.1
Average mass flow rate of outlet(kg/s) $\times 10^{-3}$		1.7191			1.9830	2.2940	2.4283	2.6075	3.2087	3.9844	4.2768	4.5711



Chapter 6

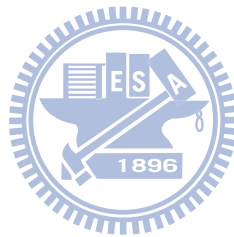
Conclusions and Future Works

6.1 Conclusions

In this study, the effects of fuels with LHV on the performance of an annular MGT power system were assessed experimentally and numerically. The proposed system in this study has the potential to reduce the size of a distributed power supply system for biogas and enhance its popularization. The numerical analyses show that the cool air flows via dilution holes on liners were fully functioned and chamber design did not cause hot spots on the chamber liner or make the temperature of exhaust gas exceed the maximum allowable that temperature of the turbine wheels can tolerate. In the experiments, the proposed MGT power system was operated successfully under each test condition; minimum composition to the fuel with the LHV was roughly 60% CH₄ with 40% CO₂. The power output was around 170W at 85,000 RPM as 90% CH₄ with 10% CO₂ was used and 70W at 60,000 RPM as 70% CH₄ with 30% CO₂ was used. When a critical limit of 60% CH₄ was reached, the power output was extremely low. Furthermore, the theoretical Brayton cycle efficiency and electric efficiency of the MGT were calculated as 23% and 10%, respectively. The electric efficiency might be improved by replacing the generator as suggested in Future Works section. This study presents a novel distributed power supply system that can utilize renewable biogas. The completed micro biogas power supply system is small, low cost, easy to maintain and suited to household use.

6.2 Future Works

To reduce fuel supply pressure and enhance safety, fuel pipe diameter of the proposed annular MGT system can be enlarged to deliver additional volume of fuel for future studies. Moreover, the data-acquisition facilities of the MGT system can be enhanced to determine gas exhaust components. The CO concentration profile in exhaust gas can help researchers determine whether complete combustion is achieved. Furthermore, in some fields, a brushless DC motor can be utilized as a generator and actuator simultaneously. Thus, if such a generator is applied to the proposed MGT, power loss is avoidable compared to that when transmissions are used to connect the power turbine and generator.



Reference

- [1] R. J. Lawson, Computational Modeling of an Aircraft Engine Combustor to Achieve Target Exit Temperature Profiles, Proceedings of the International Gas Turbine and Aeroengine Congress and Exposition, Cincinnati, USA, 1993.
- [2] E. J. Fuller and C. E. Smith, Integrated CFD modeling of Gas Turbine Combustors, American Institute of Aeronautics and Astronautics paper, 1993.
- [3] A. Gulati, A. K. Tolpadi, G. Vandeusen, and D. L. Burrus, Effect of Dilution Air on Scalar Flowfield at Combustor Sector Exit, Journal of Propulsion Power, Vol. 11, pp. 1162-1169, 1995.
- [4] A. M. Danis, D. L. Burrus, and H. C. Mongia, Anchored CCD for Gas Turbine Combustor Design and Data Correlation, Journal of Engineering Gas Turbine Power, pp.535-545, 1997.
- [5] M. K. Lai, CFD Analysis of Liquid Spray Combustion in a Gas Turbine Combustor, Proceedings of the International Gas Turbine and Aeroengine Congress and Exposition, Orlando, USA, 1997.
- [6] P. Gooselin, S. DeChamplain, Kalla, and D. Kretschmer, Three-Dimensional CFD Analysis of a Gas Turbine Combustor, 36th AIAA Joint Propulsion Conference and Exhibition, Huntsville, USA, 2000.
- [7] W. C. Ho and L. C. Weng, Annular Combustor for Miniature Jet Engine, International Journal of Turbo and Jet Engines, pp. 105-115, 1996.
- [8] D. S. Crocker, D. Nickolaus, and C. Smith, CFD Modeling of a Gas Turbine Combustor from Compressor Exit to Turbine Inlet, Journal of Engineering Gas Turbines Power, Vol. 121, pp. 89-95, 1999.
- [9] N. C. Eccles and C. H. Priddin, Accelerated Combustor Design Using CFD, ISABE Paper-7094, 1999.
- [10] P. Birkby, R. S. Cant, and W. N. Dawes, CFD Analysis of a Complete Industry Lean Premixed Gas Turbine Combustor, ASME Paper-0131, 2000.

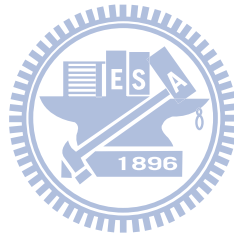
- [11] T. S. Snyder and J. F. Stewart, Application of an Advanced CFD-based Analysis System to PW6000 Combustor to Optimize Exit Temperature Distribution, ASME Paper-0064, 2001.
- [12] L. Li, X. F. Peng, and T. Liu, Combustion and Cooling Performance in an Aero-engine Annular Combustor, Applied Thermal Engineering, Vol. 25, pp. 1171-1179, 2006.
- [13] W. W. Lung, Study of Microturbine Generator System Testing Technology, NTHU Thesis, 2001.
- [14] C. H. Wang, Performance Investigation of a Microturbine Generator Set, NTHU Thesis, 2003.
- [15] <http://www.capstoneturbine.com/>
- [16] <http://www.bowmanpower.co.uk/>
- [17] <http://web.mit.edu/>
- [18] M. Wu, J. Hua, and K. Kumar, An Improved Micro-combustor Design for Micro Gas Turbine Engine and Numerical Analysis, Journal of Micromechanics and MicroEngineering, Vol. 15, pp. 1817-1823, 2005.
- [19] X. C. Shan, Z. F. Wang, Y. F. Jin, M. Wu, J. Hua, C. K. Wong, and R. Maeda, Studied on a Micro Combustor for Gas Turbine Engines, Journal of Micromechanics and MicroEngineering, Vol. 15, pp. 215-221, 2005.
- [20] P. Jan, R. Dominiek, and V. Filip, Development of an Axial Microturbine for a Portable Gas Turbine Generator, Journal of Micromechanics and Microengineering, pp. 190-195, 2003.
- [21] K. Isomura, S. Tanaka, S. Togo, H. Kanebako, M. Murayama, N. Saji, F. Sato, and M. Esashi, Development of Micromachine Gas Turbine for Portable Power Generation, JSME International Journal Series B: Fluids and Thermal Engineering, Vol. 47, pp. 459-464, 2004.
- [22] D. B. Shiung, Flow field and Performance Testing of a Micro Gas Turbine Annular Combustor, NCKU Thesis, 1995.
- [23] Y. C. Li, Design and Performance Testing of a Miniature Gas Turbine's Annular Combustor, NCKU Thesis, 2004.
- [24] U. Kruger, J. Huren, S. Hoffmann, W. Krebs, P. Flohr, and D. Bohn, Prediction and Measurement of Thermoacoustic Improvements in Gas

Turbines with Annular Combustor Systems, *Journal of Engineering for Gas Turbines and Power*, Vol. 123, pp. 557-566, 2001.

- [25] D. Yamashita, K. Kuwabara, K. Tatsumi, and K. Nakabe, Experimental Evaluation on Low-heating Value Fuel Acceptability of Micro Gas Turbine System Operation, *The 16th International Symposium on Transport Phenomena*, pp. 1-7, Prague, 2005.
- [26] H. Cohen, C. F. C. Roger, and H. I. H. Saravanamuttoo, *Gas Turbine Theory*, 3rd Edition, Longman, London, 1987.
- [27] A. J. Fawke and H. I. H. Saravanamuttoo, M. Holmes, Experimental Verification of a Digital Computer Simulation Method for Predicting Gas Turbine Dynamic Behaviors, *Inst. Mechanism Engineering Progress*, 1972.
- [28] T. Shobeiri, Digital Computer Simulation of the Dynamic Operating Behaviors of Gas Turbines, *Brown Boveri Rec*, 1987.
- [29] A. Hussain and H. Seifi, Dynamic Modeling of a Single Shaft Gas Turbine, *Proc. of the IFAC symposium on control of power plants and power systems, Munich Germany*, pp. 43-48, 1992.
- [30] Q. Z. Al-Hamdan and M. S. Y. Ebaid, Modeling and Simulation Turbine Engine for Power Generation, *Journal of Engineering for Gas Turbines and Power*, pp.302-311, 2006.
- [31] W. W. Hung, Dynamic simulation of gas turbine generating unit, *IEE Proceedings, Part C: Generation, Transmission and Distribution*, Vol. 138, pp. 342-350, 1991.
- [32] W. J. Rowen, Simplified Mathematical Representations of Heavy Duty Gas Turbine, *Journal of Engineering Power*, pp. 865-869, 1983.
- [33] L. N. Hannett and A. H. Khan, Combustion Turbine Dynamic Model Validation from Tests, *IEEE Transactions of Power System*, Vol. 8, pp. 152-158, 1993.
- [34] G. Crosa, G. Ferrari, and A. Ttucco, Modeling and Recoupling the control loops in a Heavy-duty Gas-turbine Plant, *Proceedings of the International Gas Turbine and Aeroengine Congress and Exposition, Houston, USA*
- [35] S. M. Camporeale, B. Fortunato, and A. Dumas, Dynamic Modeling and Control of Regenerative Gas Turbines, *Proceedings of the International*

- Gas Turbine and Aeroengine Congress and Exposition, Stockholm, Sweden, 1998.
- [36] C. H. Yang, D. H. Wu, C. C. Chung, and C. H. Chen, Optimal Design of a Methane-used Combustor: Applying CFD Modeling, The 3rd International Green Energy Conference, Vasteras, Sweden, 2007.
- [37] [http://www.sym.com.tw/chi/generator spec](http://www.sym.com.tw/chi/generator_spec)
- [38] <http://www.ni.com/>
- [39] R. W. Fox and A. T. McDonald, Introduction to Fluid Mechanics, John Wiley and Sons, Canada, 1994.
- [40] S. J. Kline and F. McClintock, Describing Uncertainties in Single-Sample Experiments, Mechanical Engineering, Vol. 104, pp. 250-260, 1982.
- [41] K. K. Kuo, Principles of Combustion, John Wiley and Sons, Canada, 1986.
- [42] CFD-ACE+ V2004 Modules Manual V1, ESI group company.
- [43] M. N. Pham, Studies in Structures of Laminar Hydrocarbon Flames, Ph. D. Dissertation, University of California, San Diego, 1992.
- [44] F. M. White, Viscous Fluid Flow, 2nd ed., McGraw-Hill, Inc., 1991.
- [45] J. R. Andrews and O. Biblarz, Temperature Dependence of Gas Properties in Polynomial Form, Naval Postgraduate School, California, 1981.
- [46] Engineering Properties of Steel, Philip D. Harvey, American Society for Metals, Metals Park, Ohio 44073, 1982.
- [47] <http://www.cfdrc.com/>
- [48] CFD-ACE+ V2004 User Manual, ESI group company.
- [49] Patankar, Numerical heat transfer and fluid flow, Taylor & Francies, 1980.
- [50] Ferziger and Peric, Computational methods for fluid dynamics, 3rd ed., Springer, 2002.
- [51] W. I. Rowen, Simplified Mathematical Representation of Single Shaft Gas Turbine in Mechanical Drive Service, Turbomach. Int., pp. 26-32, 1992.

- [52] W. L. William and L. H. Chin, Gas Turbine Engine Testing Education at Western Michigan University, Western Michigan University, Kalamazoo, MI, 49008, 2007.
- [53] R. E. Sonntag, Fundamentals of Thermodynamics, John Wiley & Sons, INC, 2003.
- [54] MW 54 Assembly and Operation Manual, Wren Turbine Ltd.



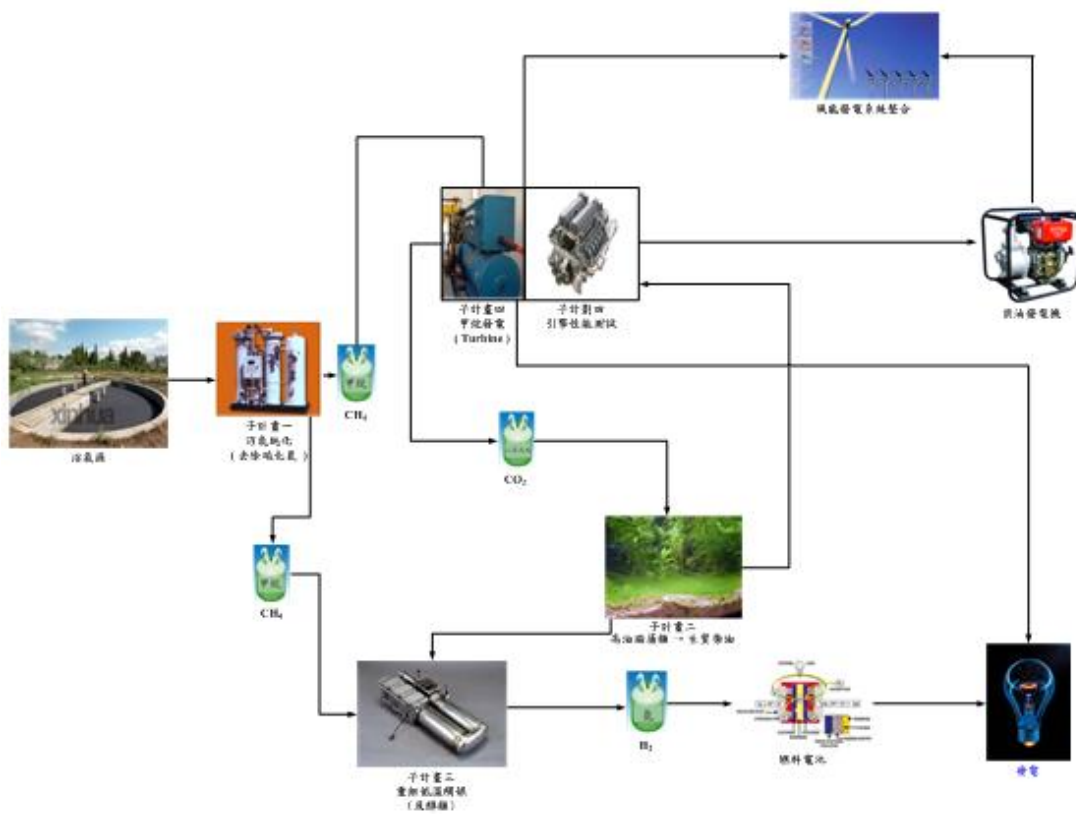


Figure 1.1: The structure of project.

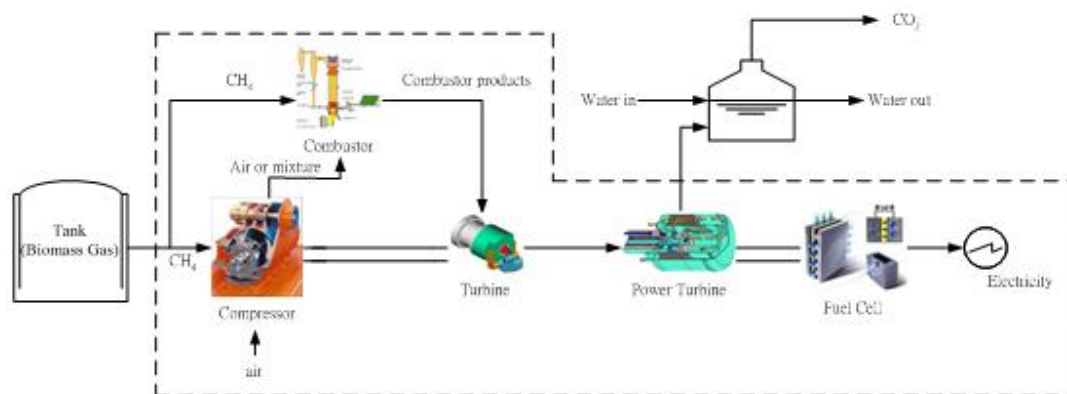


Figure 1.2: The basic structure of the MGT generator.

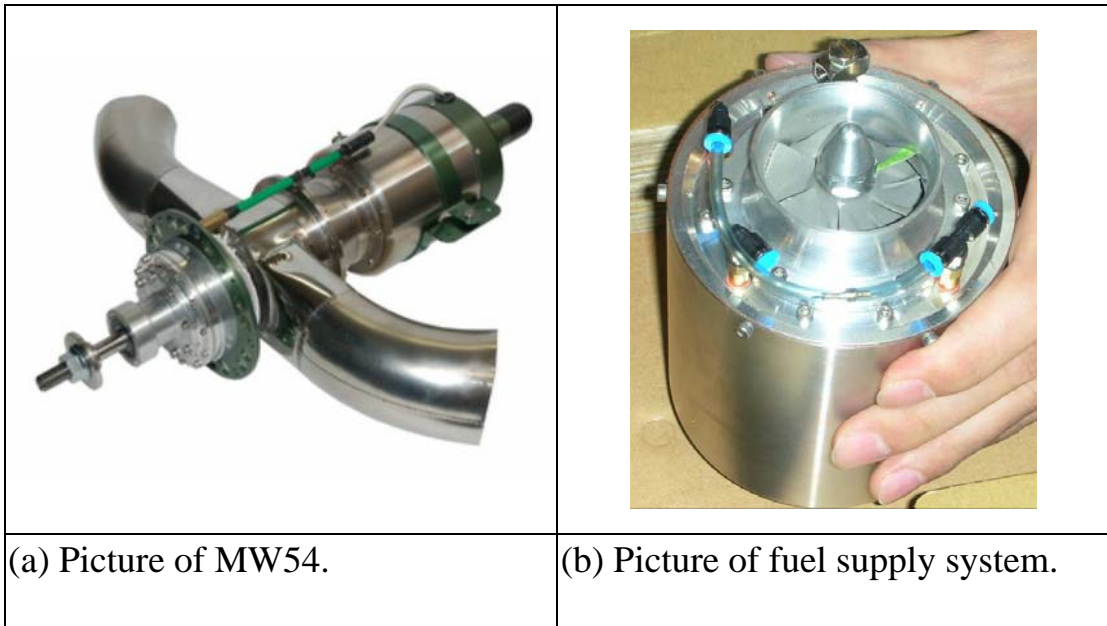
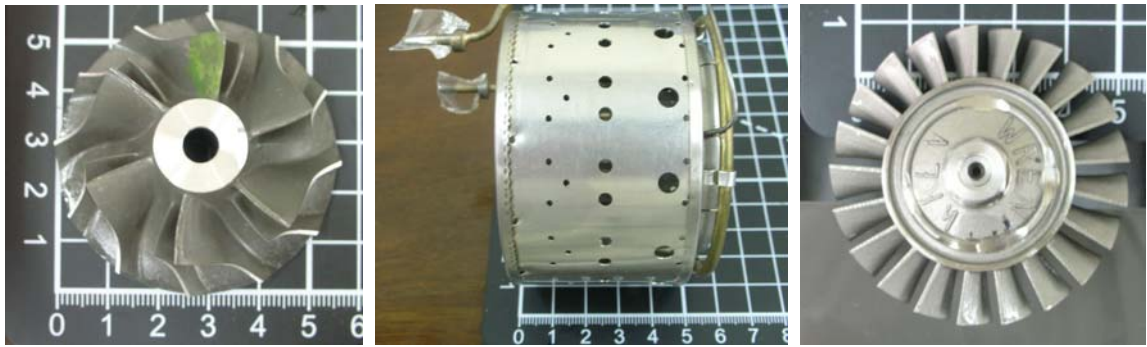


Figure 1.3: Pictures of the adopted micro gas turbine.





(a)

(b)

(c)

Figure 2.1: Pictures of the major parts in MGT. (a) Compressor (b) Combustion chamber (c) Turbine wheel

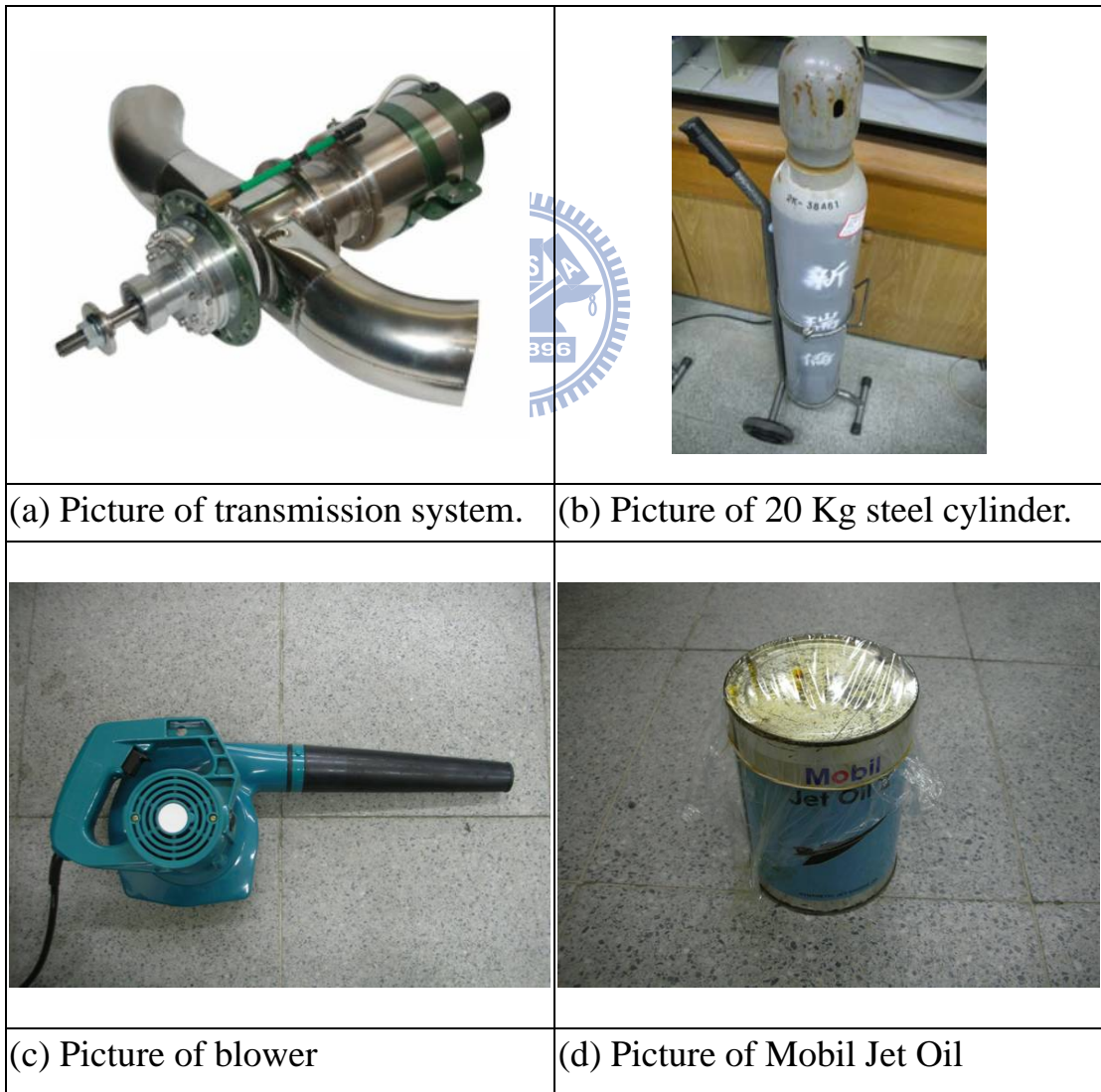
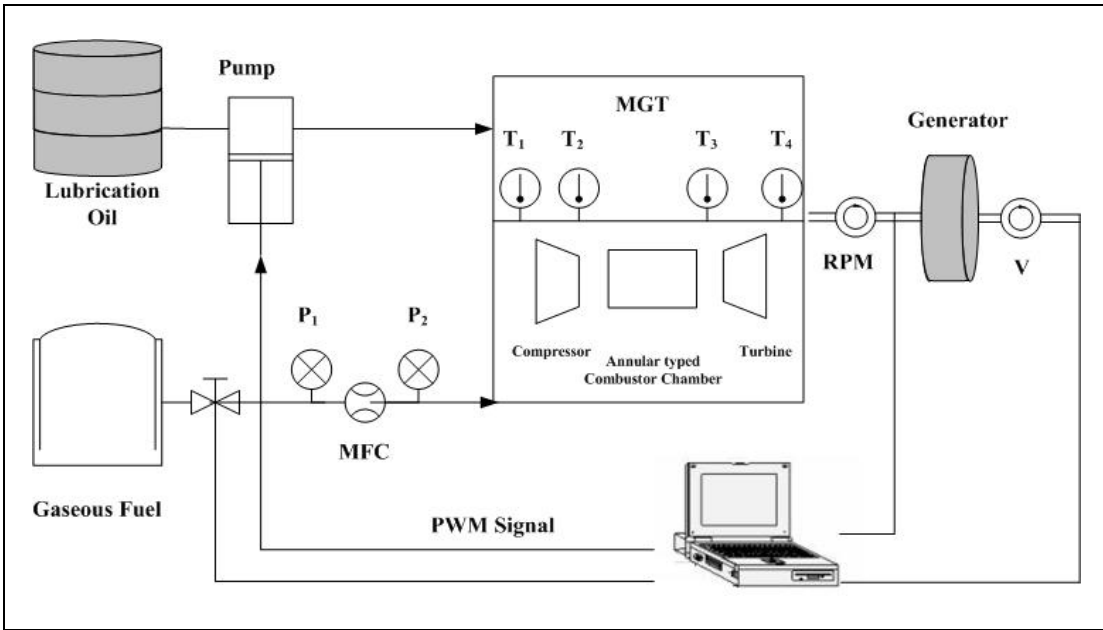
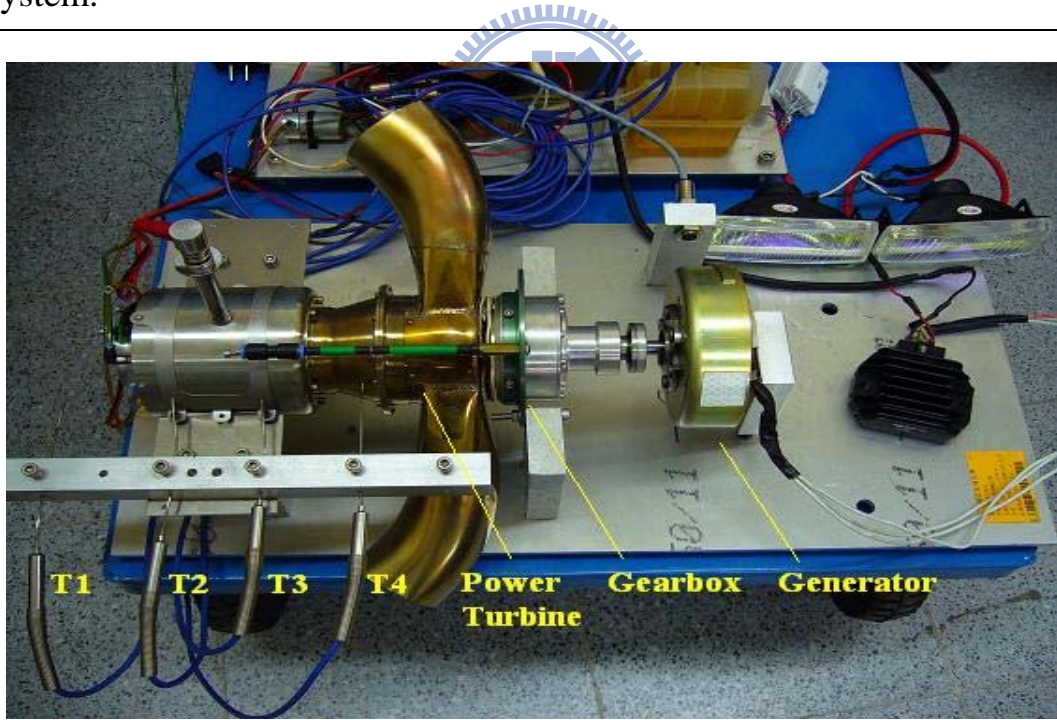


Figure 2.2: Pictures of experimental facilities in proposed MGT system.



(a) Schematic of the experimental configuration for proposed MGT system.



(b) Picture of the suspended test stand.

Figure 2.3: Schematic of experiment layout.



(a) Picture of the CompactDAQ Chassis.



(b) Picture of Analog Input Module.

(c) Picture of Analog Output Module.



(d) Picture of Thermocouple Differential Analog Input Module.

(e) Picture of Simultaneous Analog Input Module.

Figure 2.4: Pictures of data acquisition devices.

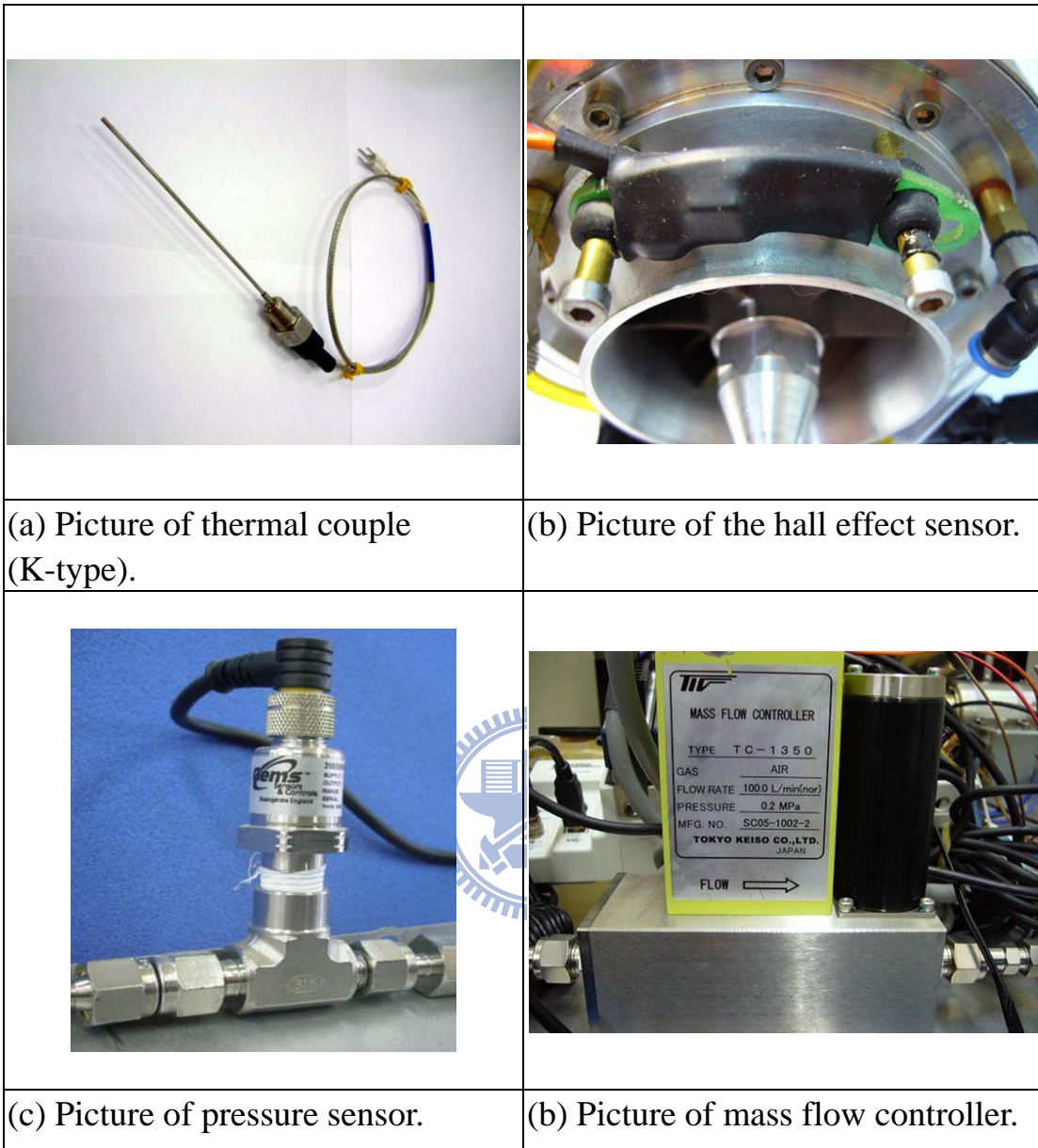


Figure 2.5: Pictures of sensors and actuators for the proposed MGT system.

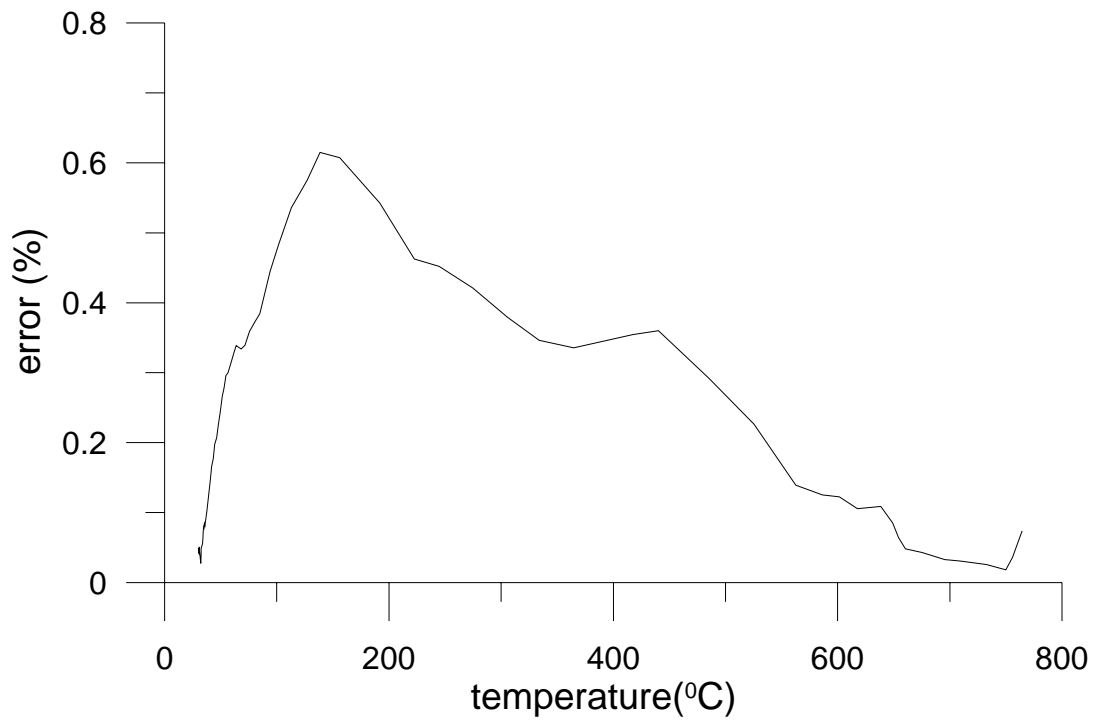
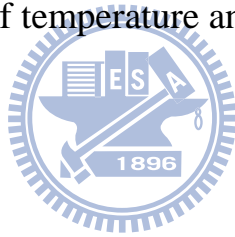


Figure 2.6: The relationship of temperature and error.



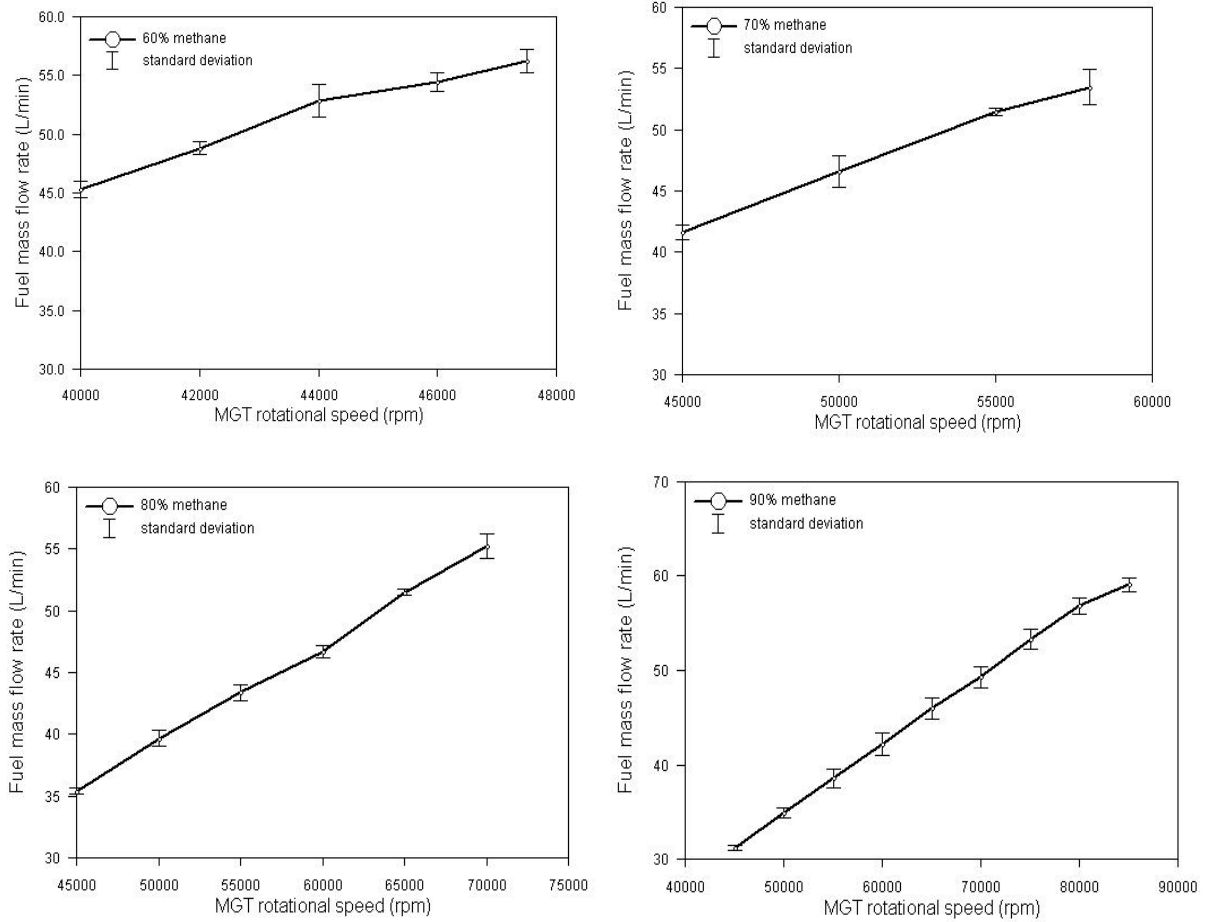


Figure 2.7: Experimental error bars for CH₄:CO₂ mixing ratios: (a) 60% CH₄ to 40% CO₂, (b) 70% CH₄ to 30% CO₂, (c) 80% CH₄ to 20% CO₂, and (d) 90% CH₄ to 10% CO₂.

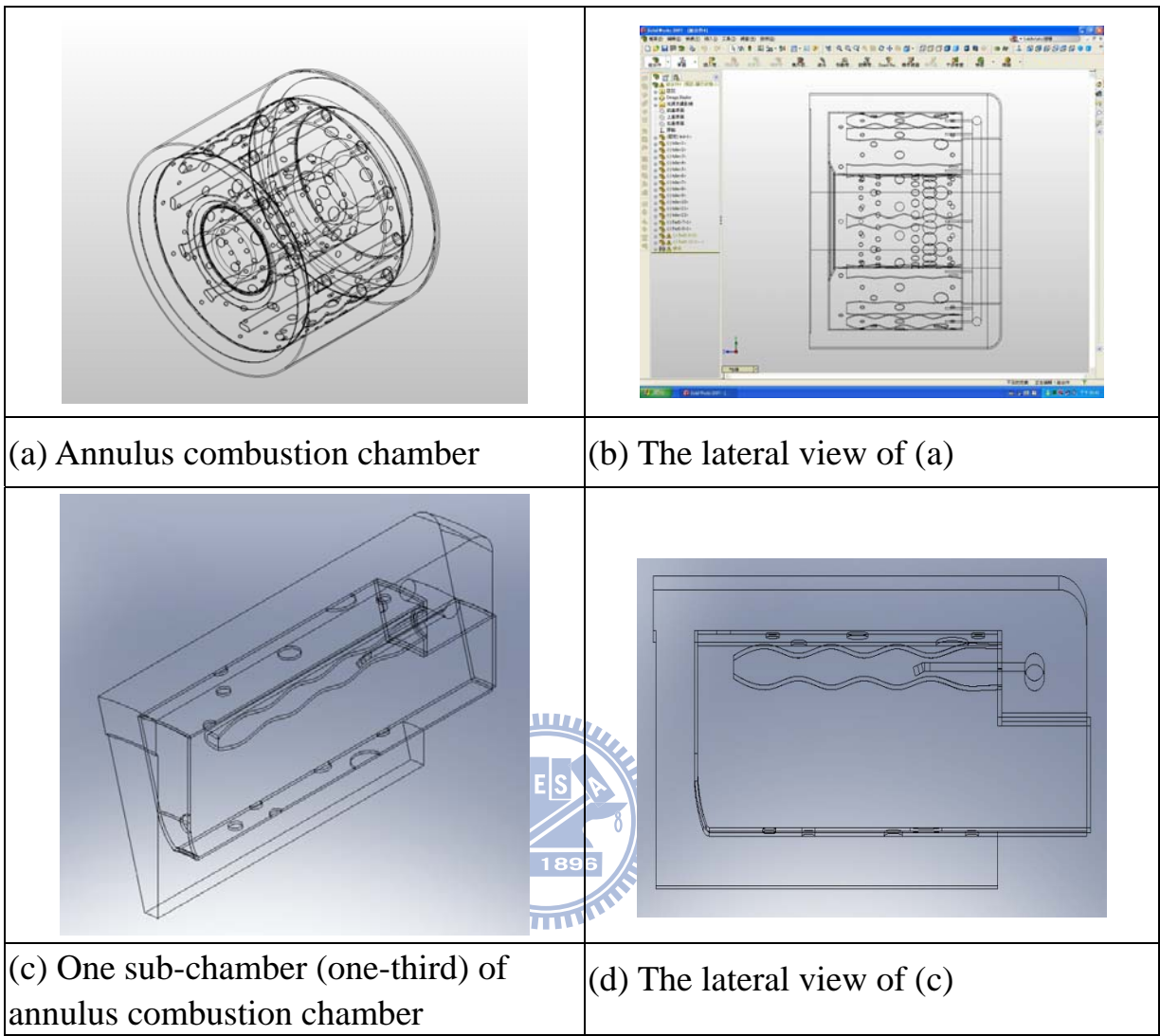


Figure 3.1: The simplifying procedure of model domain illustrated by software Solid Works.

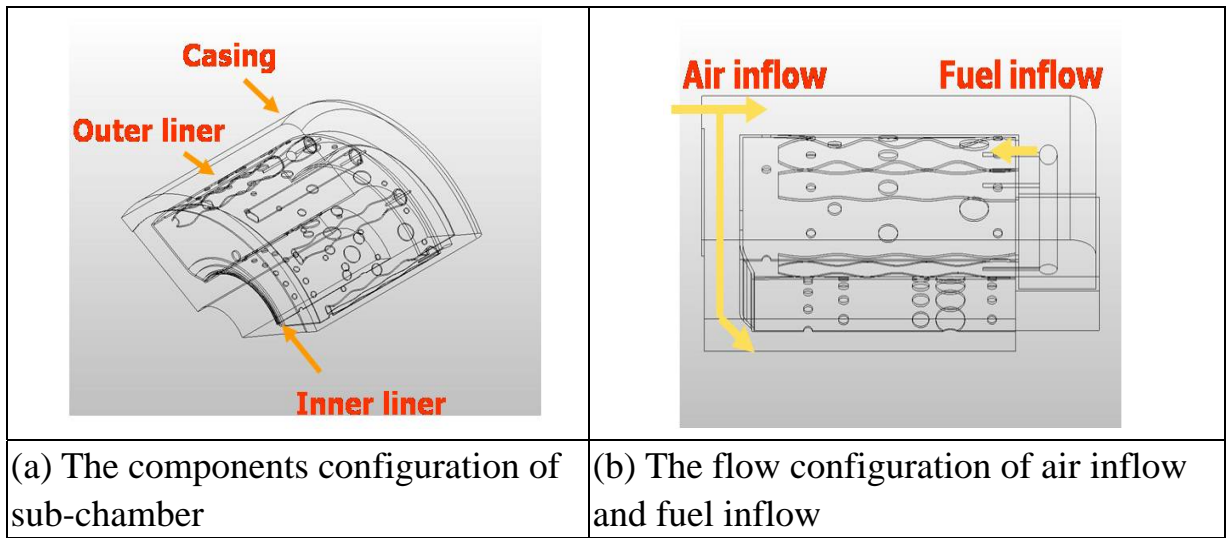


Fig. 3.2 The configurations of a sub-chamber.

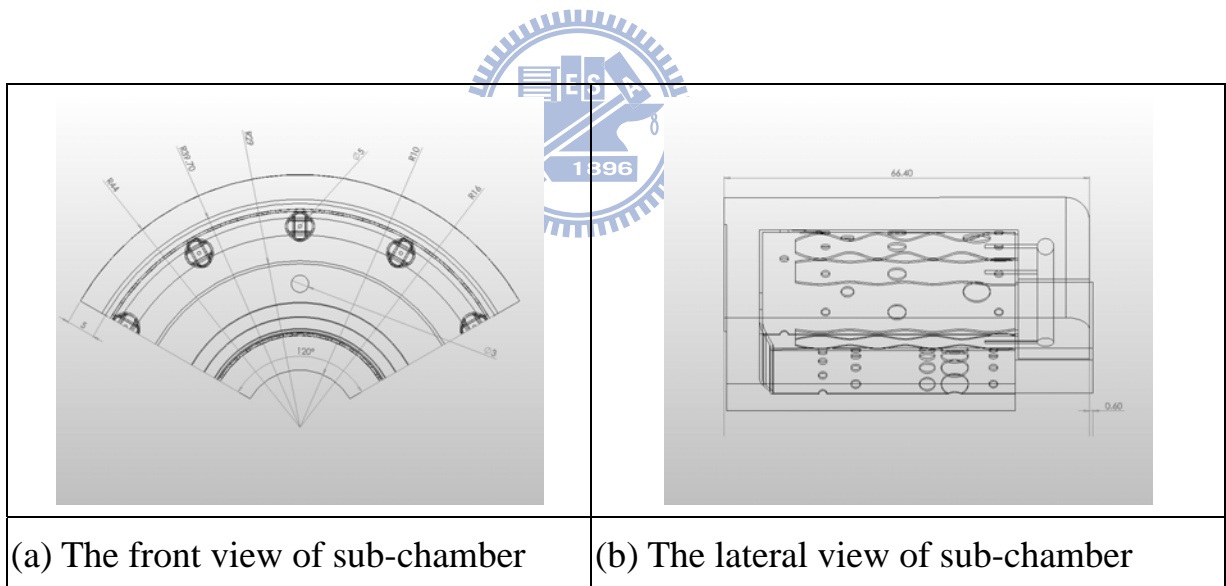
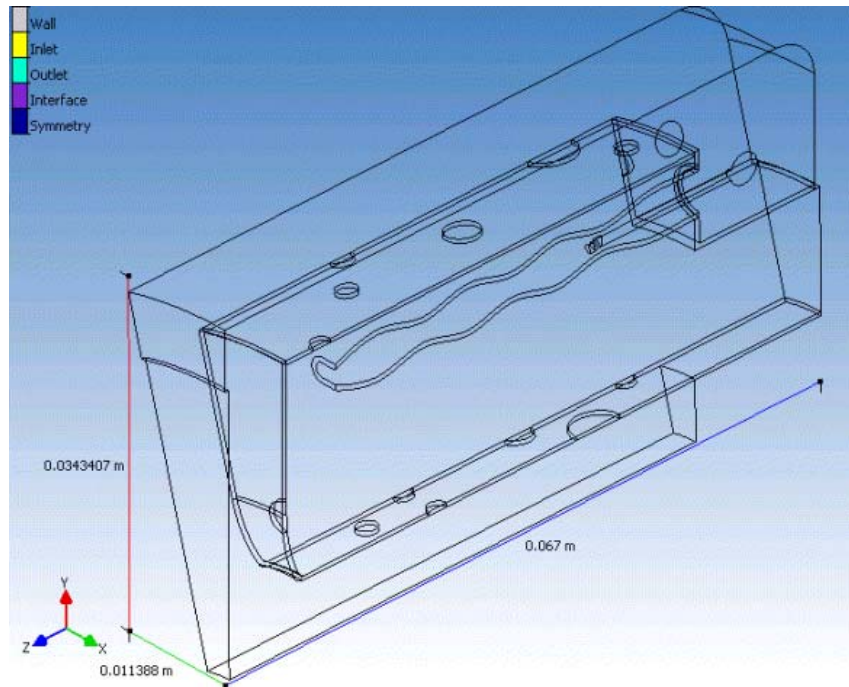
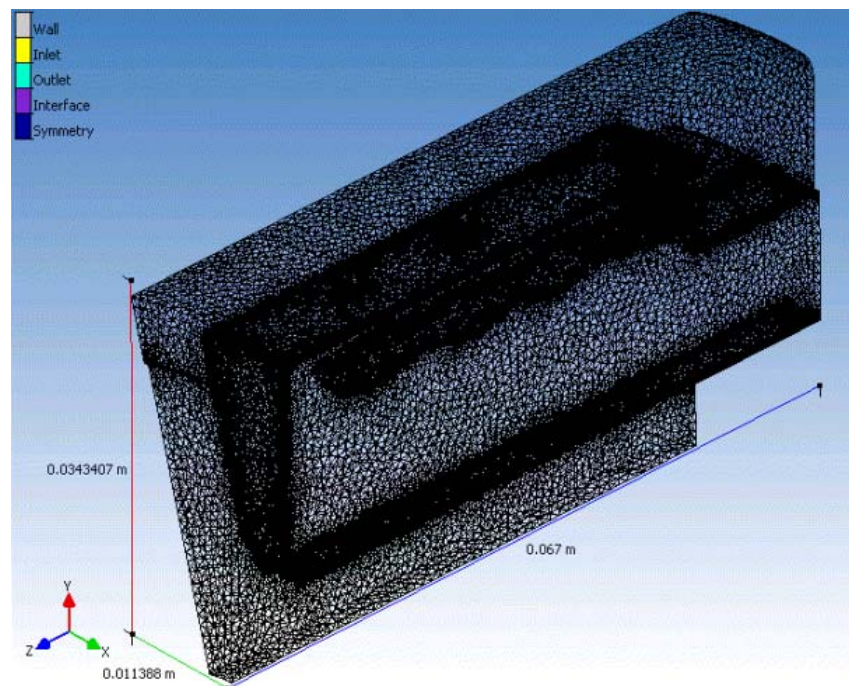


Fig. 3.3 The size specification of sub-chamber.



(a) Model domain of combustor



(b) Grids generation

Fig. 3.4 Grids generation for numerical computation.

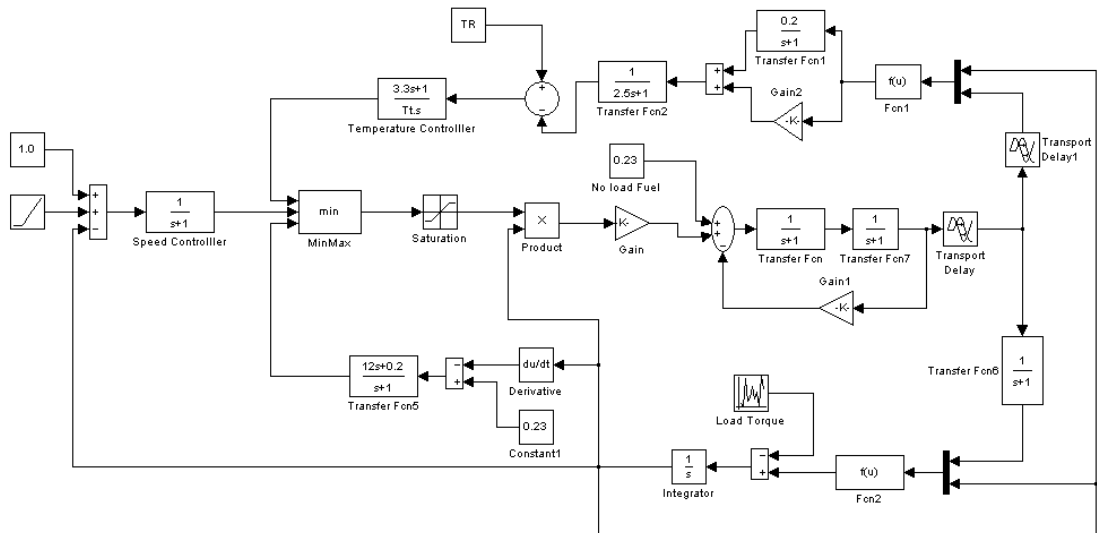
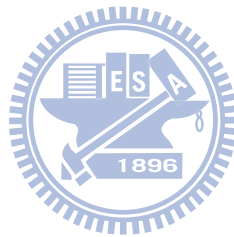


Fig. 4.1 Simulation model of micro gas turbine in SIMULINK.



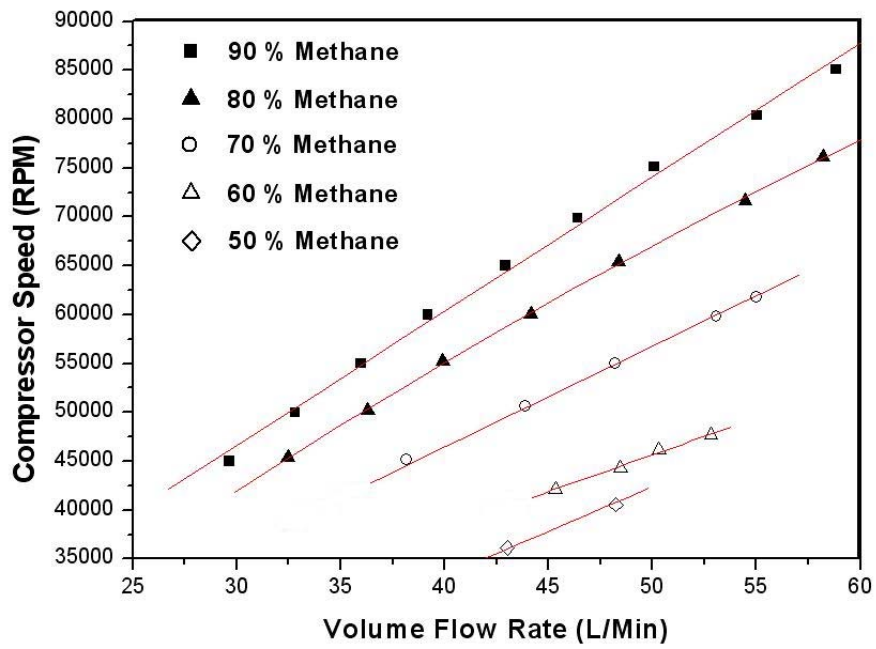
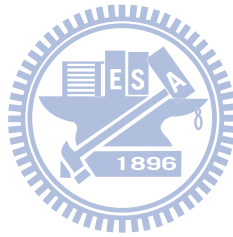


Figure 5.1: Volume flow rate for fuels with LHV fuels at various RPMs.



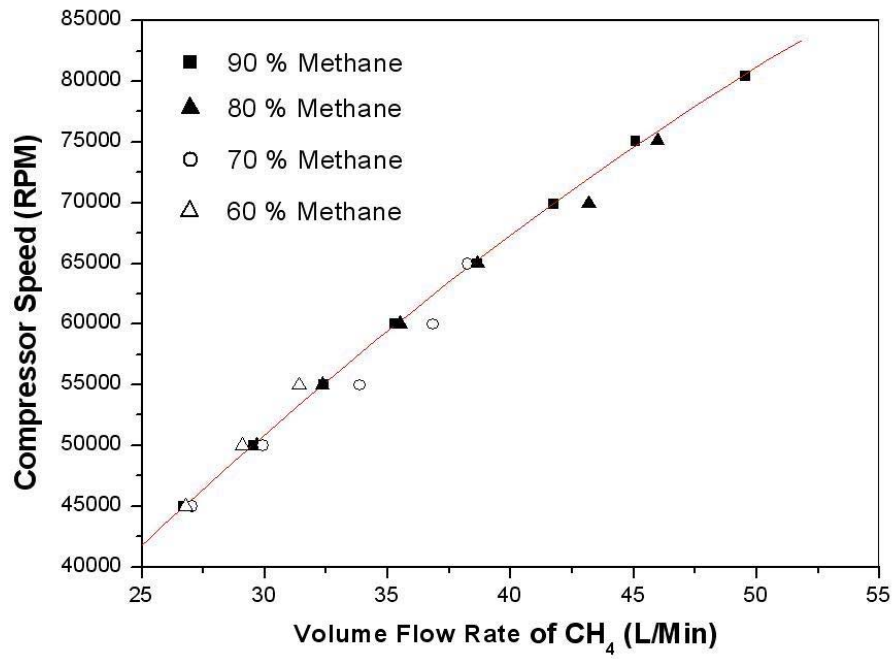
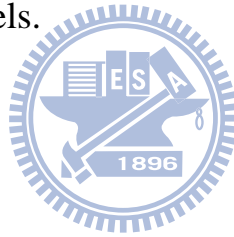
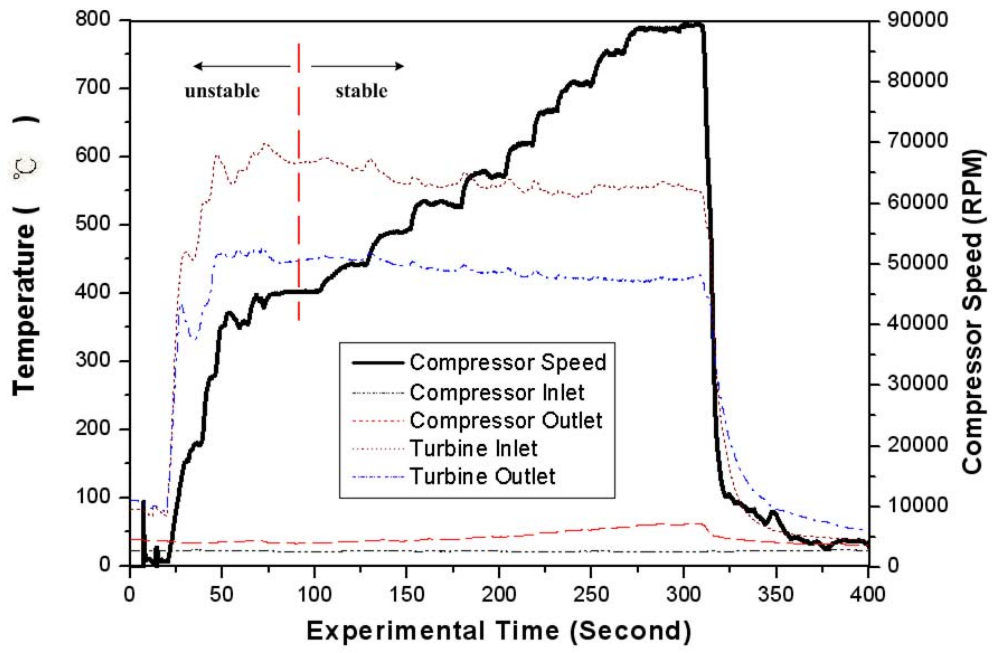
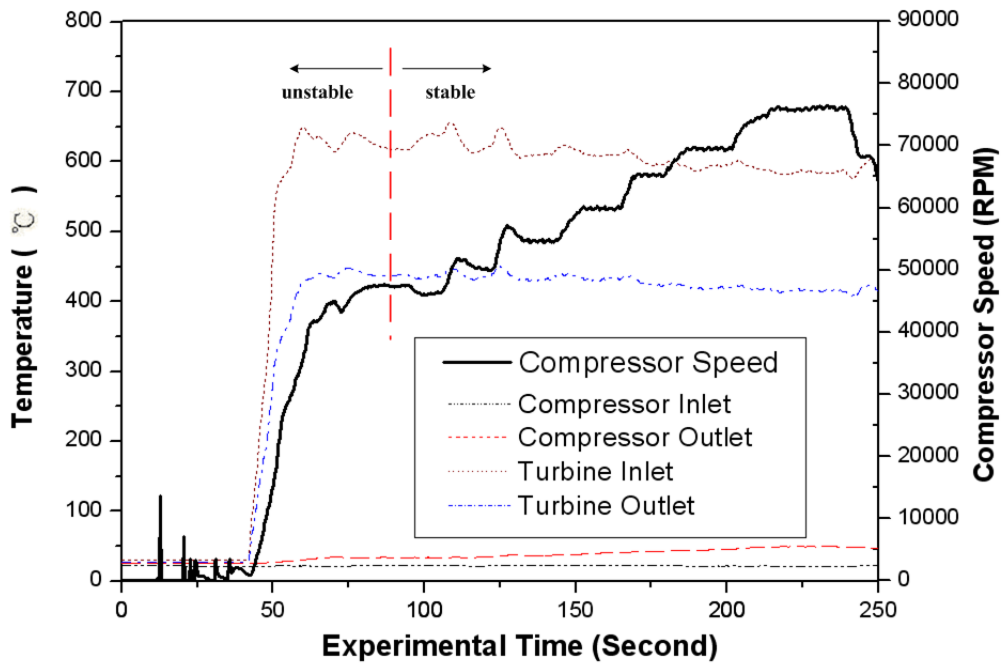


Figure 5.2: Compressor speed vs. volume flow rate of CH₄ with different concentrations of methane fuels.

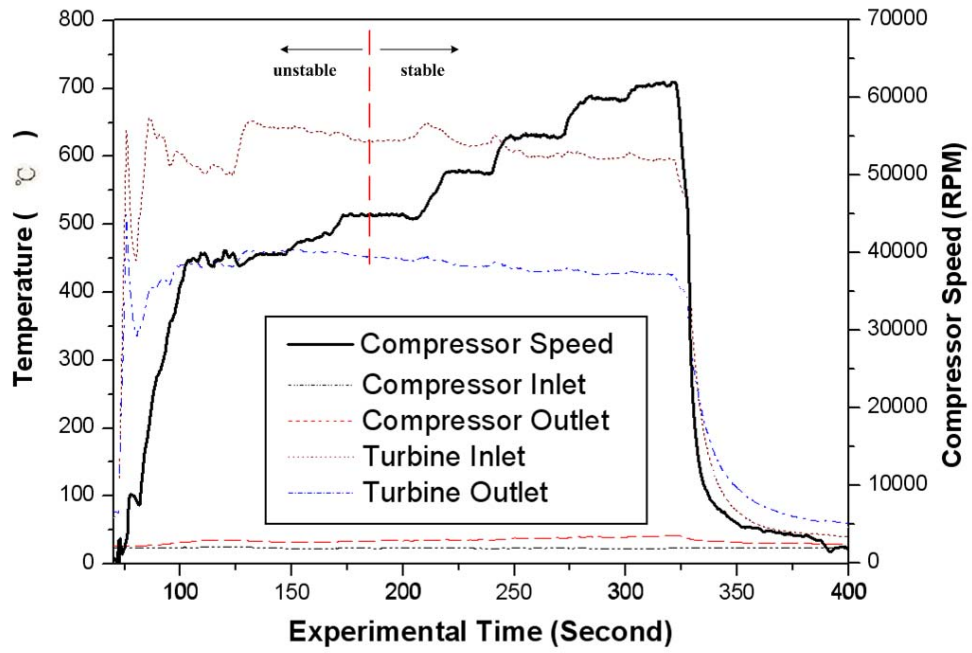




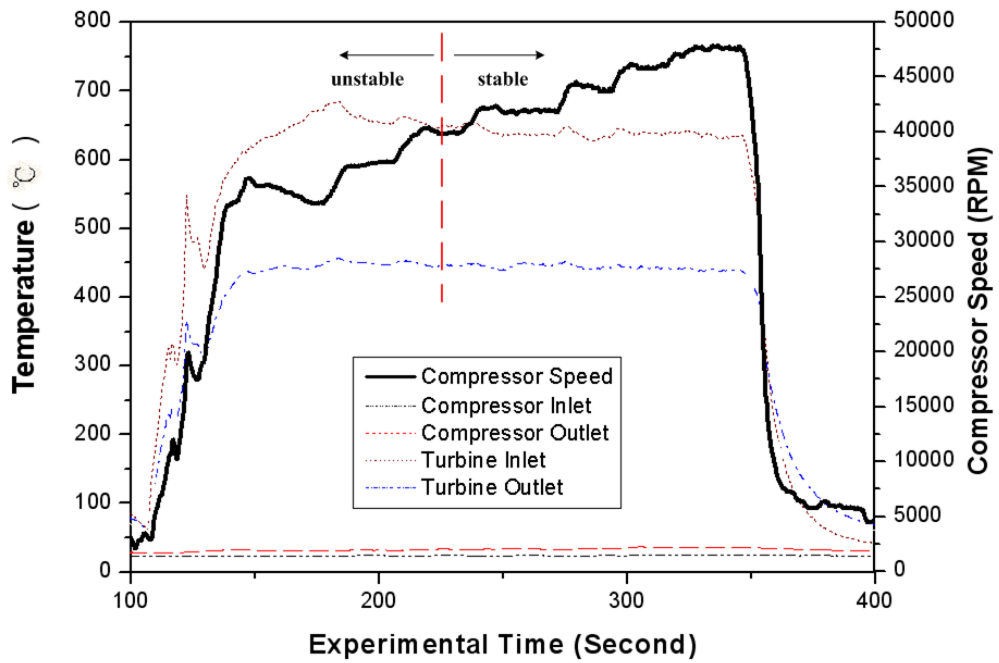
(a)



(b)



(c)



(d)

Figure 5.3: Temperatures at different positions in the MGT (a) Fuel with 90% CH₄; (b) Fuel with 80% CH₄; (c) Fuel with 70% CH₄; (d) Fuel with 60% CH₄.

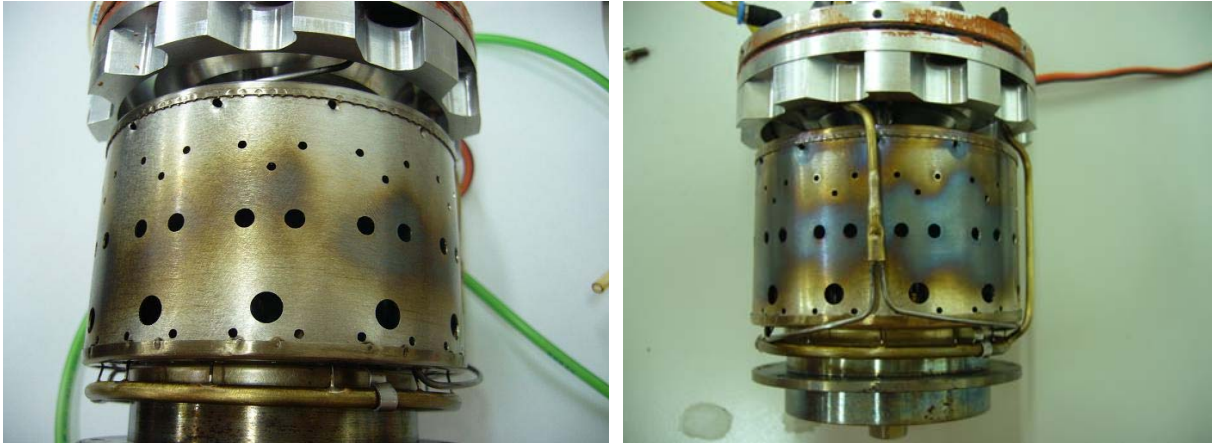
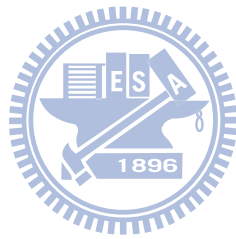


Figure 5.4: (a) Combustion chamber (oil). (b) Combustion chamber using 70% CH_4 (gas).



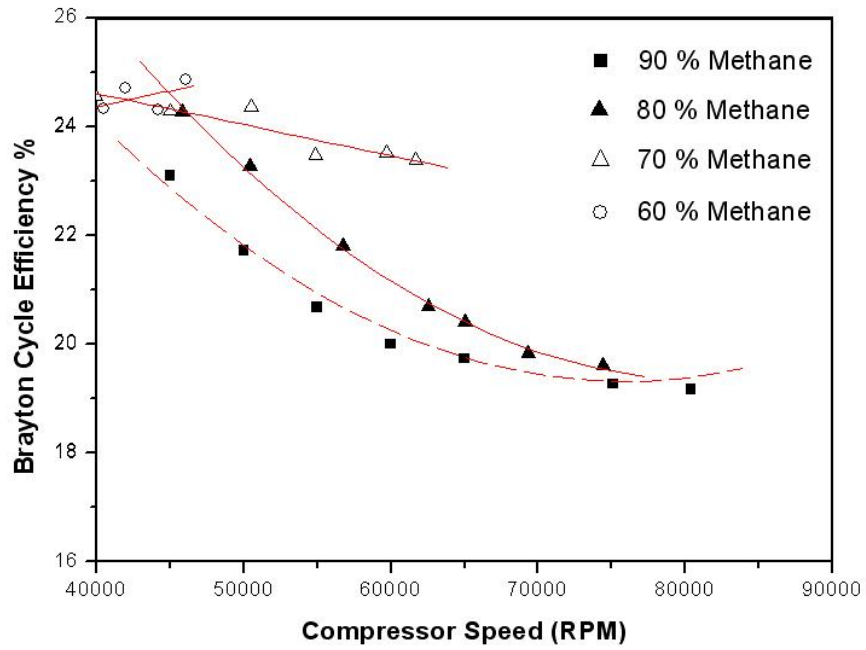
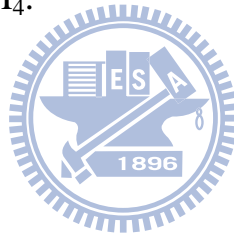


Figure 5.5: Brayton cycle efficiency of different compressors speed with different concentrations of CH₄.



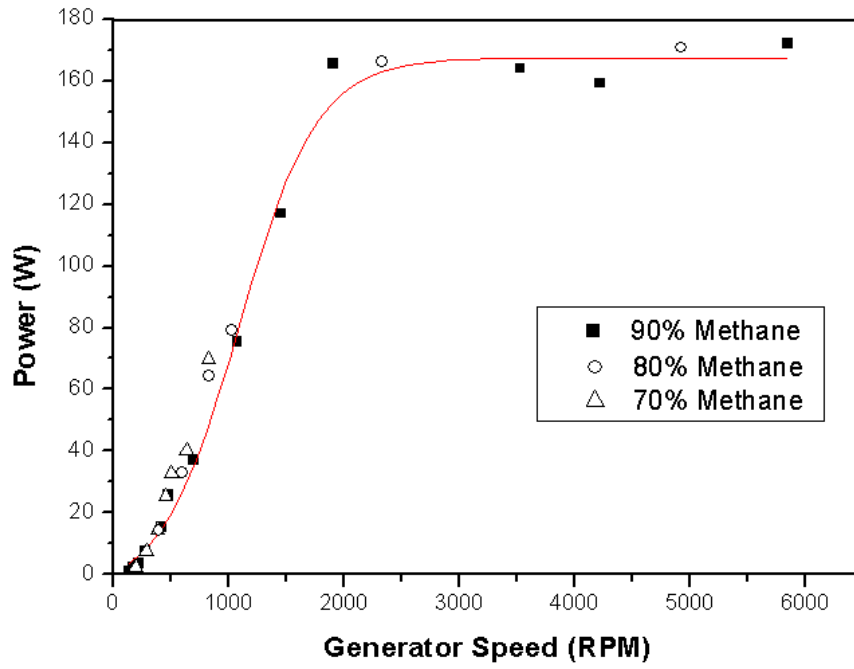
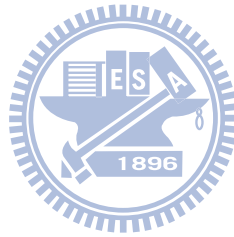
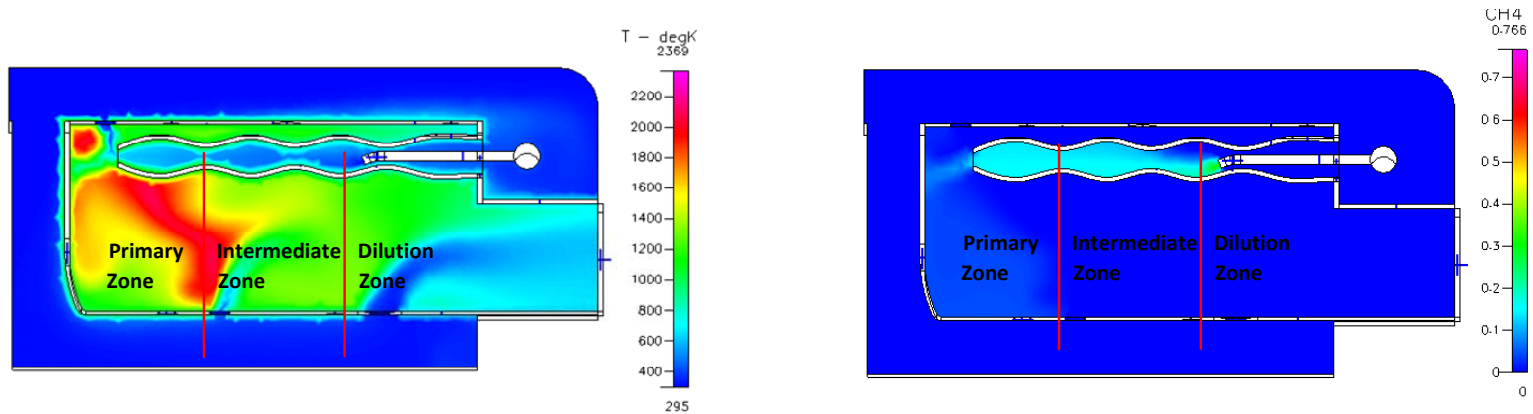


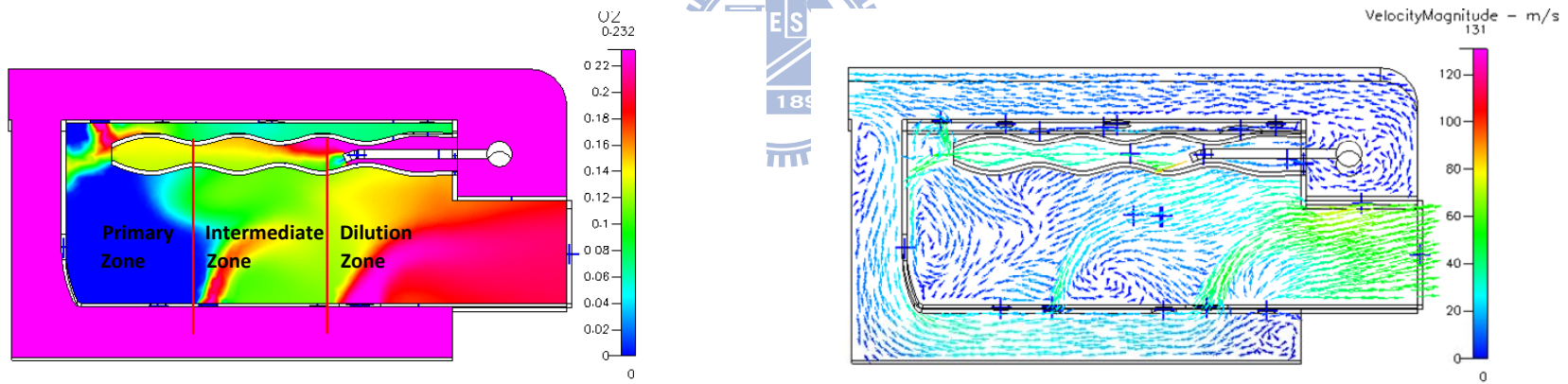
Figure 5.6: Output power for different generator rotation speeds with different LHV fuel.





(a) Temperature distribution in combustor.

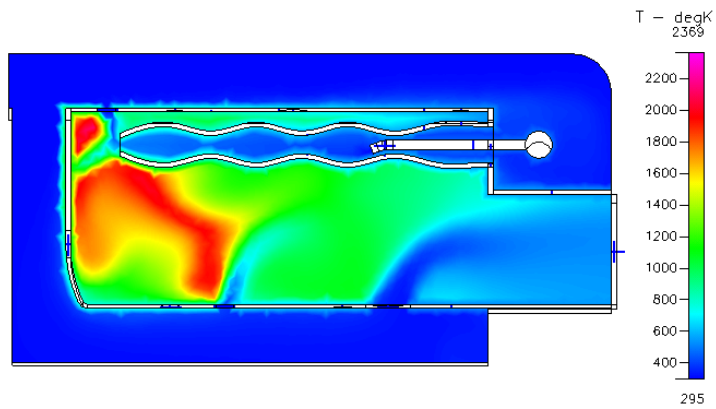
(b) Mass fraction distribution of methane.



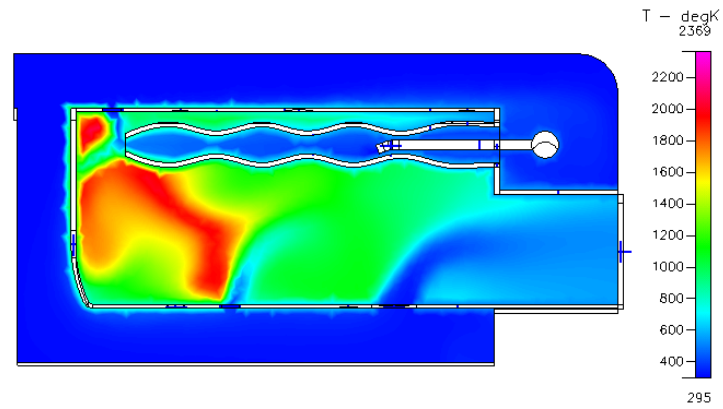
(c) Mass fraction distribution of oxygen.

(d) Distributions of velocity flow field.

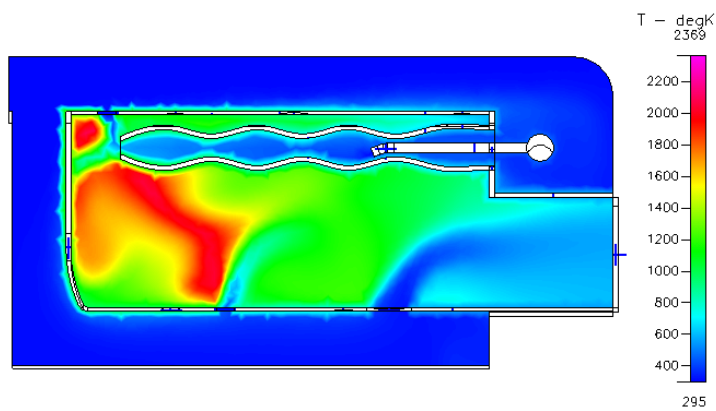
Figure 5.7: Simulation results of applying 60% methane fuel at rotation speed 45000RPM.



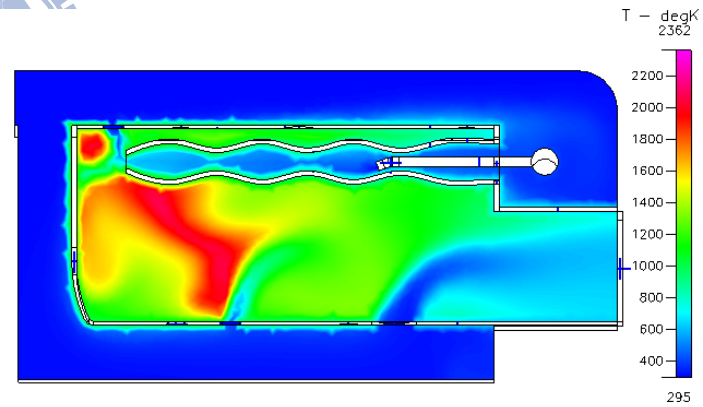
(a) 90% methane concentration.



(b) 80% methane concentration.

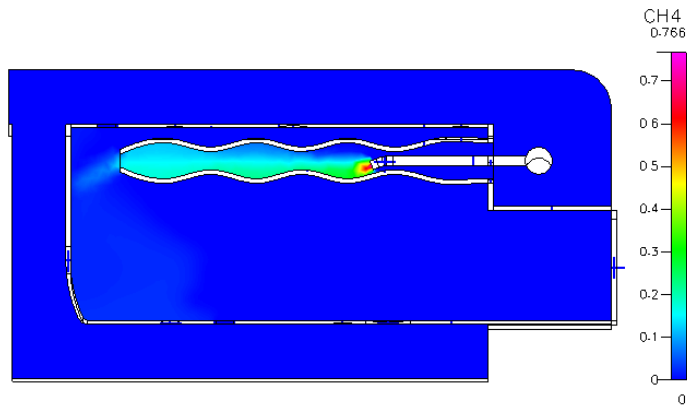


(c) 70% methane concentration.

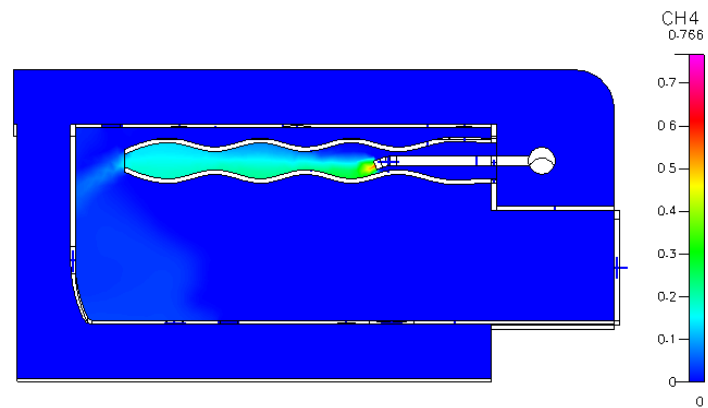


(d) 60% methane concentration.

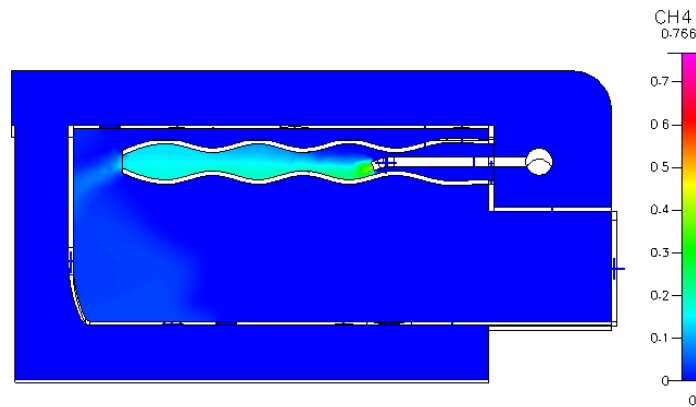
Figure 5.8: Distribution of temperature for different concentration of methane at 45000 RPM.



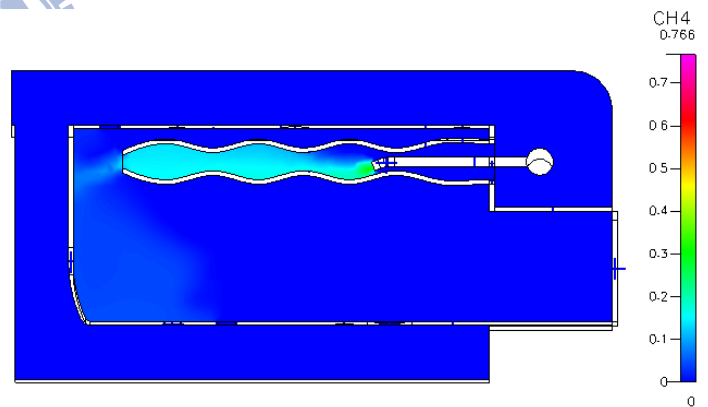
(a) 90% methane concentration.



(b) 80% methane concentration.

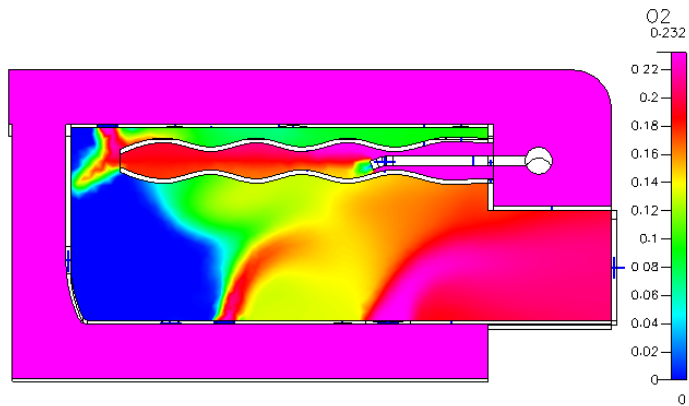


(c) 70% methane concentration.

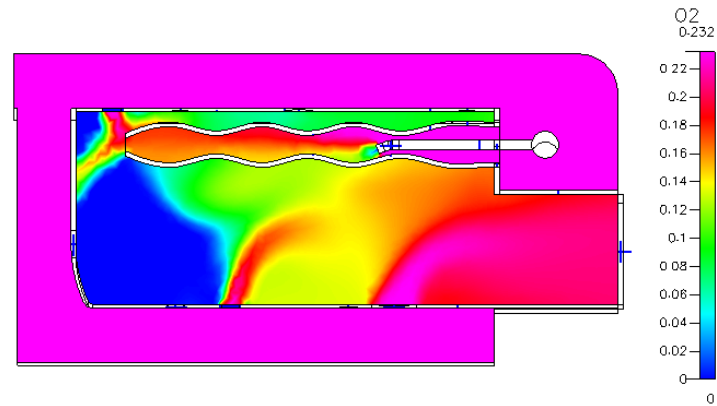


(d) 60% methane concentration.

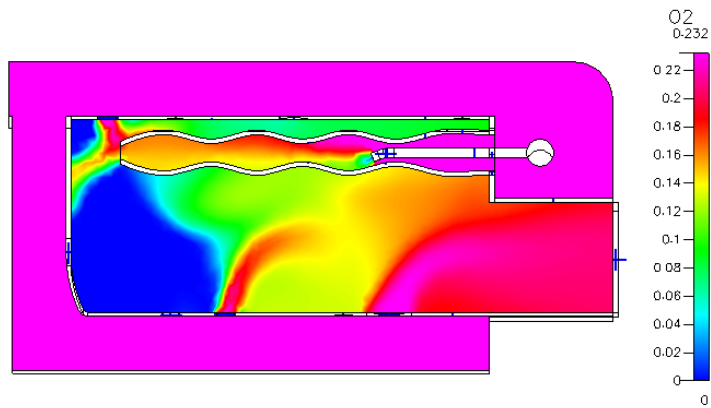
Figure 5.9: Distributions of CH₄ mass fraction for different concentration of methane at 45000 RPM.



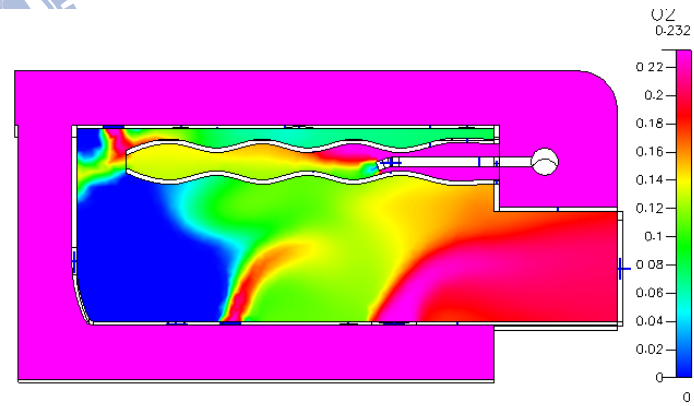
(a) 90% methane concentration.



(b) 80% methane concentration.

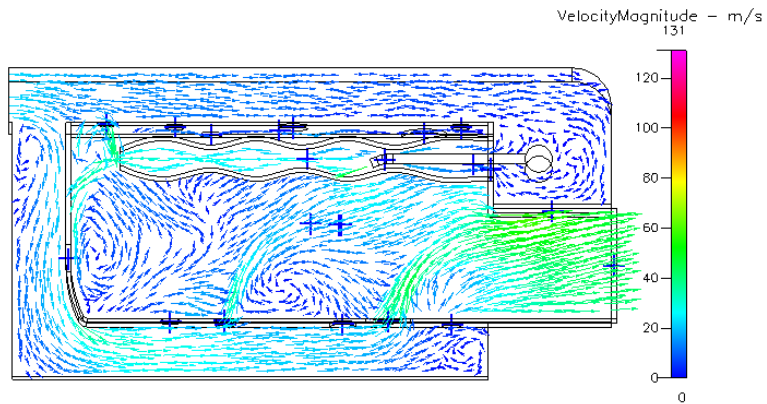


(c) 70% methane concentration.

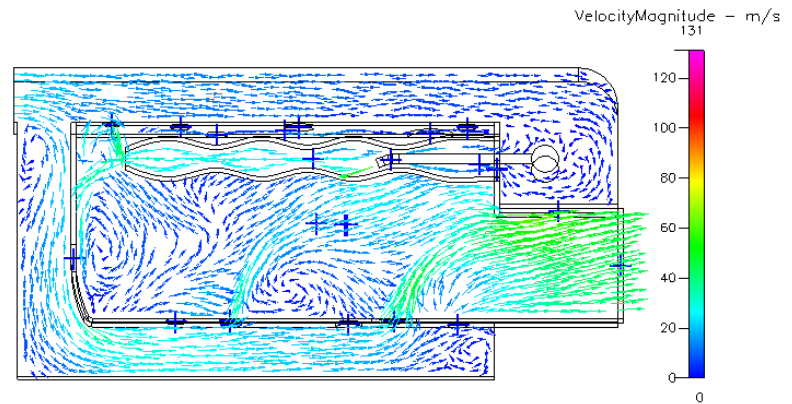


(d) 60% methane concentration.

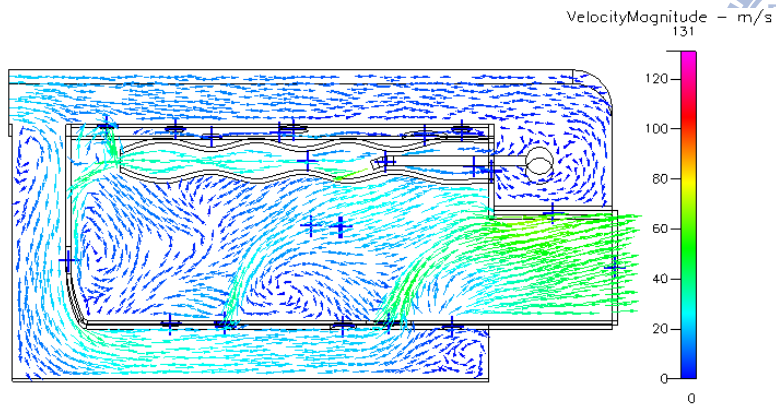
Figure 5.10: Distributions of O_2 mass fraction for different concentration of methane at 45000 RPM.



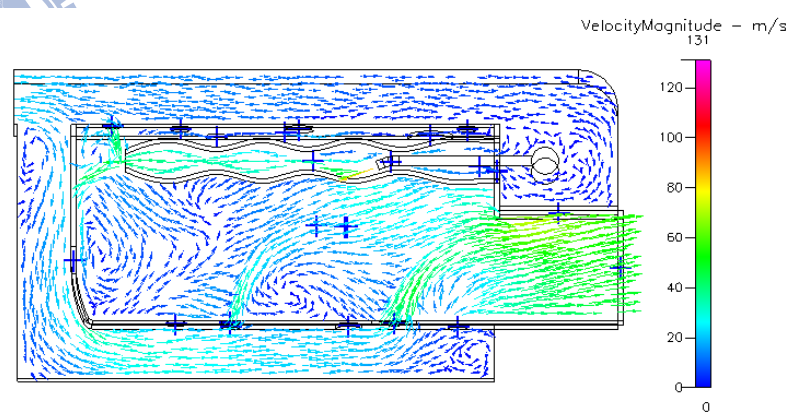
(a) 90% methane concentration.



(b) 80% methane concentration.

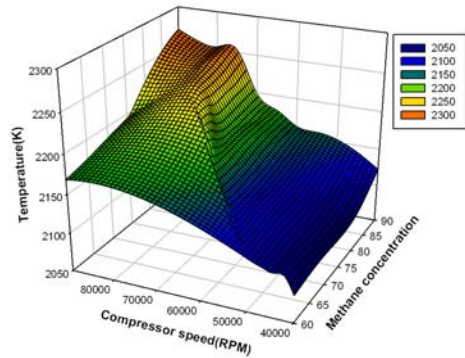


(c) 70% methane concentration.

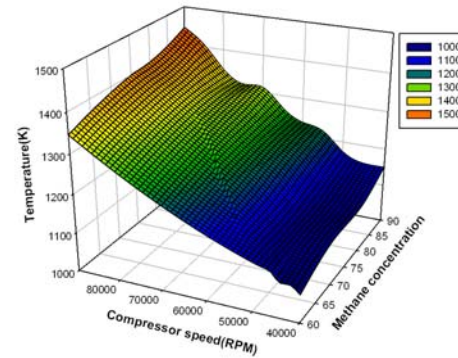


(d) 60% methane concentration.

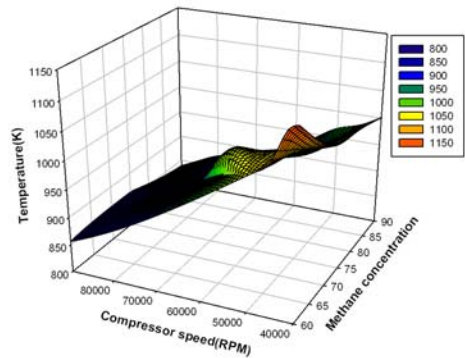
Figure 5.11: Velocity vector of flow field for different concentration of methane at 45000 RPM.



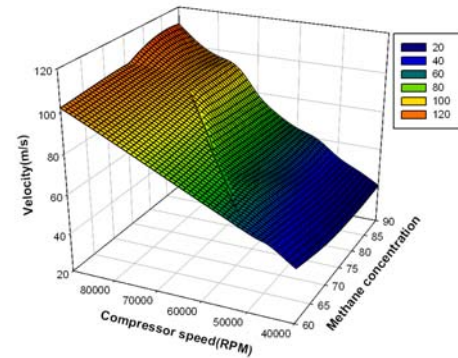
(a) Maximum temperature in combustor



(b) Maximum temperature on liner walls

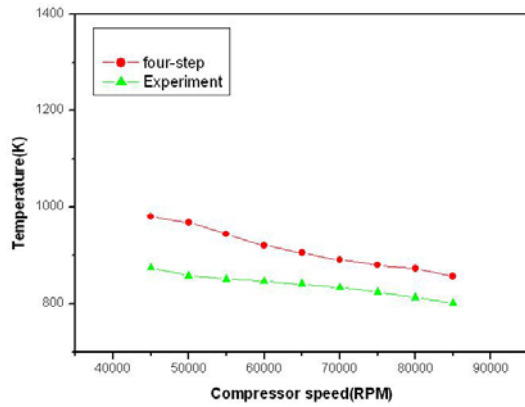


(c) Outlet maximum temperature

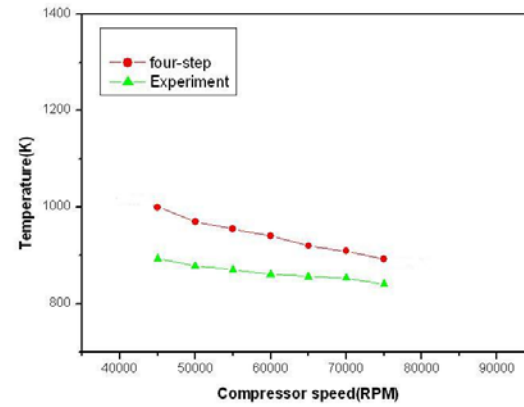


(d) Outlet maximum velocity

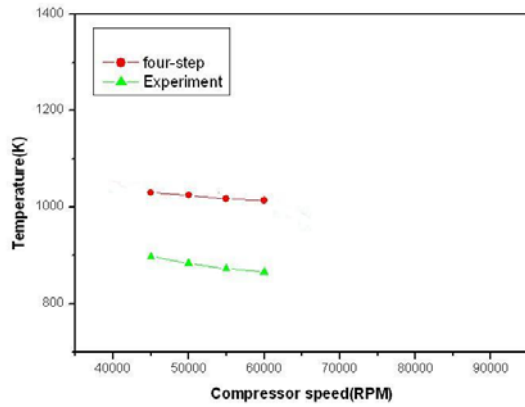
Figure 5.12: Curved chart with different methane concentration and different compressor speed



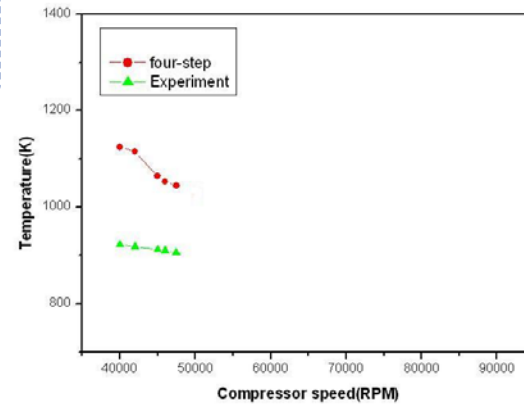
(a) 90% CH₄ to 10% CO₂



(b) 80% CH₄ to 20% CO₂;



(c) 70% CH₄ to 30% CO₂;



(d) 60% CH₄ to 40% CO₂

Figure 5.13: Maximum temperature at combustor outlet for different fuel

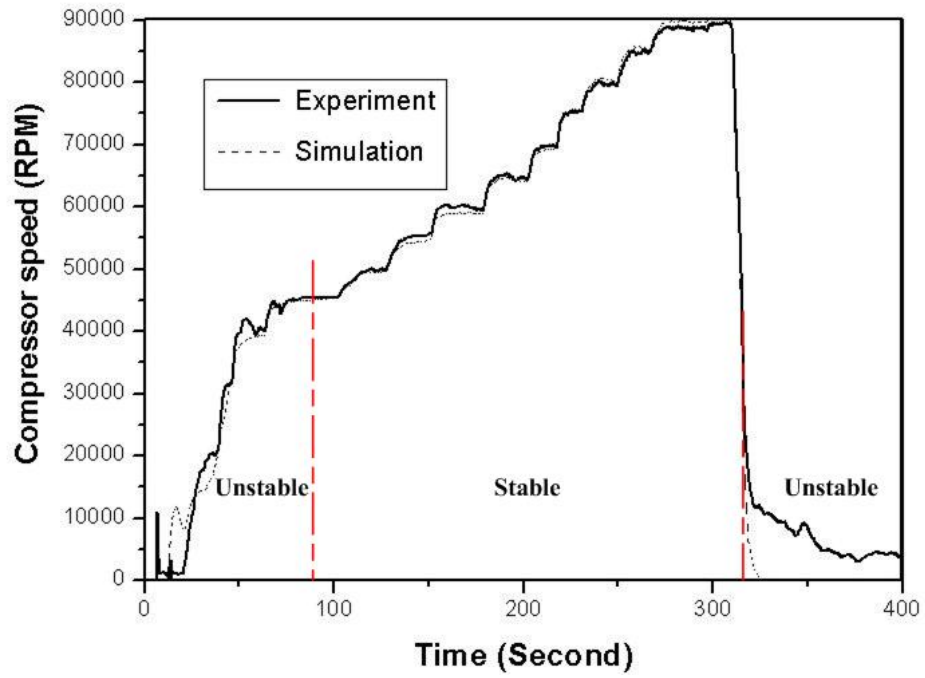
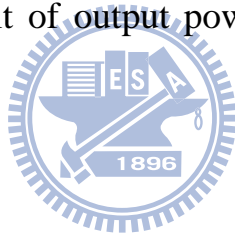


Figure 5.14: Numerical result of output power for different generator rotation speeds with 90% CH₄.



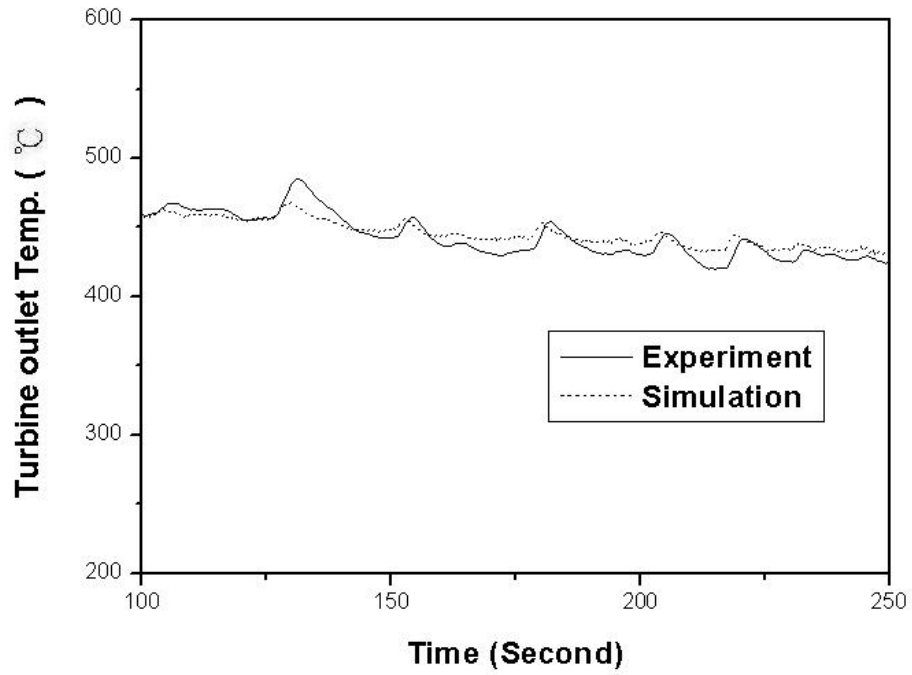
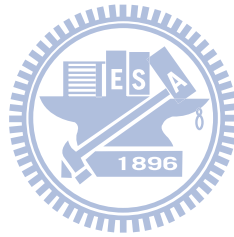


Figure 5.15: Numerical result of turbine outlet temperature versus experimental time.



Publications

1. R. F. Fung, C. H. Yang, and J. L. Ha, Hysteresis Identification and Dynamic Responses of the Impact Drive Mechanism, *Journal of Sound and Vibration*, Vol. 283, pp. 943-956, 2005.
2. C. H. Yang, M. T. Yu, C. H. Chen, and C. H. Chen, Performance Simulation and Thermal Stress Analysis of Ceramic Recuperators by SiC and MAS, *Numerical Heat Transfer, Part A: Applications*, Vol.53, pp.709-725, 2008.
3. C. H. Yang, D. H. Wu, and C. H. Chen, Numerical Performance Analysis of an Annular Miniature Gas Turbine Power System using Fuels with Low Heating Values, *International Journal of Numerical Methods for Heat and Fluid Flow*, 2009. (Accepted)
4. C. H. Yang, C. C. Lee, J. H. Hsiao, and C. H. Chen, Numerical Analysis and Experiment Investigations to an Annular Micro Gas Turbine Power System using Fuels with Low Heating Values, *Science in China Series E-Technological Sciences*, 2009. (Accepted)
5. R. F. Fung, C. H. Yang, S. C. Hsien, and J. L. Ha, Identification of the Piezoelectric Actuator with Hysteresis Based on Real-Coded Genetic Algorithm, 第十三屆自動化技術研討會
6. R. F. Fung, and C. H. Yang, Hysteresis Identification and Dynamic

Simulations of an Impact Drive Mechanism, 中國機械工程學會第二十屆全國學術研討會.

7. 馮榮豐、楊竣翔、韓長富，磁滯與摩擦力考慮的奈米定位，物理雙月刊。

8. C. H. Yang., D. H. Wu, and C. H. Chen, Optimal Design of a methane-used combustor: applying CFD Modeling, The 3rd International Green Conference, June 17-21, Vasteras, Sweden, 2007.

9. C. H. Yang, R. H. Hsiao, and C. H. Chen, An Improved Numerical Model Analysis and Experiment Investigations to a Methane-used Annular-type Micro Gas Turbine Power System, The Tenth World Renewable Energy Congress, July 20-23, Glasgow, Scotland, UK, 2008.

